Strong-field scattering of two spinning black holes: Numerical relativity versus post-Minkowskian gravity

Piero Rettegno,[1,2,*] Geraint Pratten,[2,†] Lucy M. Thomas,[2,‡] Patricia Schmidt,[2,§] and Thibault Damour[3,‖]

[1]*INFN Sezione di Torino, Via P. Giuria 1, 10125 Torino, Italy*
[2]*School of Physics and Astronomy and Institute for Gravitational Wave Astronomy, University of Birmingham, Edgbaston, Birmingham B15 2TT, United Kingdom*
[3]*Institut des Hautes Etudes Scientifiques, 91440 Bures-sur-Yvette, France*

(Received 14 July 2023; accepted 30 October 2023; published 6 December 2023)

Highly accurate models of the gravitational wave signal from coalescing compact binaries are built by completing analytical computations of the binary dynamics with nonperturbative information from numerical relativity (NR) simulations. In this paper we present four sets of NR simulations of equal-mass black hole binaries that undergo strong-field scattering: (i) we reproduce and extend the nonspinning simulations first presented in [Damour *et al.*, Strong-field scattering of two black holes: Numerics versus analytics, Phys. Rev. D **89**, 081503 (2014).]; (ii) we compute two suites of nonspinning simulations at higher energies, probing stronger field interactions; (iii) we present a series of *spinning* simulations including, for the first time, unequal-spin configurations. When comparing the NR scattering angles to analytical predictions based on state-of-the-art post-Minkowskian (PM) calculations, we find that PM-expanded scattering angles show poor convergence towards NR data. By contrast, a resummed computation of scattering angles via a spin-dependent, radiation-reacted, effective-one-body potential shows excellent agreement for both nonspinning and spinning configurations.

DOI: 10.1103/PhysRevD.108.124016

I. INTRODUCTION

The detection and characterisation of gravitational wave (GW) observations [1–5] from compact binary coalescences relies on theoretical predictions of the emitted signal. Highly accurate models of coalescing compact binaries are a crucial requirement to perform precise measurements of the properties of black holes (BHs) and neutron stars, to determine their underlying astrophysical distributions and to perform tests of General Relativity in the strong-field regime. Such waveform models are generally built using both analytical and numerical approximations to Einstein's equations for a binary system in quasicircular orbits.

Numerical Relativity (NR) simulations of quasi-circular binaries [6–13] provide the most accurate representation of the emitted waveform, especially during the plunge, merger and ringdown phases. Such simulations can be used to build NR surrogates [14–16], whose main limitation is their restricted parameter space coverage.

Semianalytical GW approximants, such as effective-one-body (EOB) [17–21] and phenomenological models [22–26], use a combination of numerical and analytical information. These approximants generally make use of the post-Newtonian (PN) expansion [27–41], which assumes small velocities ($v/c \ll 1$) together with weak fields [$GM/(rc^2) \ll 1$], making it apt to describe quasicircular inspirals. However, with the improving sensitivity of current detectors and ongoing development of a third generation of GW detectors [42–44], the possibility of detecting eccentric binaries and hyperbolic encounters has risen in prominence [45–48]. The detection and characterization of binaries on noncircular orbits is thought to be a powerful tracer for constraining the formation and evolution channels of astrophysical BHs [49–56].

Analytical models of noncircular binaries cannot solely rely on the PN approximation, as the two bodies could already possess high velocities at large separations. In these situations, the post-Minkowskian (PM) approximation [57,58], which only assumes weak fields [$GM/(rc^2) \ll 1$] while allowing for large velocities, is more appropriate. PM contributions have been computed

*piero.rettegno@to.infn.it
†g.pratten@bham.ac.uk
‡lthomas@star.sr.bham.ac.uk
§p.schmidt@bham.ac.uk
‖damour@ihes.fr

using various approaches to gravitational scattering, such as scattering amplitudes (see, e.g., [59–70]), eikonalization (e.g., [71–74]), effective field theory (e.g., [75–81]), and worldline (classical or quantum) field theory (e.g., [82–88]). The resulting terms can be incorporated into semianalytic models to improve their accuracy for binaries on eccentric and hyperbolic orbits [89–95]. At the same time, numerical results are necessary to determine the accuracy and validity of these approximations. Whilst a large suite of numerical simulations of binary black holes (BBHs) on eccentric orbits have been performed [47,96–103], there are comparatively few simulations regarding BBH scattering [104–108].

The aims of this paper are (i) to extend the results of Ref. [106] by performing higher-initial-energy NR simulations of equal-mass nonspinning BBH scattering;[1] (ii) to perform NR simulations of the scattering of equal-mass *spinning* BBHs, both for equal and unequal spins, aligned with the angular momentum; and (iii) to compare the so-obtained strong-field numerical scattering angles to analytical predictions based on state-of-the-art PM results.[2]

We denote the masses of the two objects as m_1 and m_2, and the individual dimensionless spins as $\chi_i = S_i/(Gm_i^2) = a_i/(Gm_i)$, $i = 1, 2$. In addition, we denote $M = m_1 + m_2$, $\mu = m_1 m_2/(m_1 + m_2)$, $\nu = \mu/M = m_1 m_2/(m_1 + m_2)^2$. All our simulations will have $m_1 = m_2$, so that $\nu = 1/4$. Throughout this paper, we denote the canonical orbital angular momentum simply as L. It is related to the total Arnowitt-Deser-Misner (ADM) angular momentum of the system, J, by

$$J = L + S_1 + S_2. \tag{1.1}$$

Unless otherwise stated, we take $G = c = 1$ and generally work with dimensionless quantities.

II. NUMERICAL RELATIVITY (NR) SIMULATIONS

We performed several sequences of nonspinning and spin-aligned NR simulations modelling the scattering of two equal mass BHs. The numerical simulations were performed using the EINSTEIN TOOLKIT (ETK) [109], an open source numerical relativity code built on the Cactus framework. The numerical setup of our simulations is broadly similar to that used in [106], though we present the details here for completeness.

We use Bowen-York initial data [110,111] computed using the TWOPUNCTURES thorn [112]. As in [106], the BHs are initially placed on the x-axis at a separation of $\pm X$ and with initial ADM linear momenta

$$\vec{P} = (P_x, P_y, P_z) = \pm P_{\rm ADM}\left(-\sqrt{1-\left(\frac{b_{\rm NR}}{2X}\right)^2}, \frac{b_{\rm NR}}{2X}, 0\right), \tag{2.1}$$

where $P_{\rm ADM} = |\vec{P}|$ and $b_{\rm NR}$ denotes an impact parameter. As in [106], we use $X = 50$ M. The Bowen-York initial data determine both the initial total ADM energy $E_{\rm in}^{\rm ADM}$ of the system, and the total initial ADM angular momentum of the system. The latter is given by the simple formula

$$J_{\rm in}^{\rm ADM} = L_{\rm in} + S_1 + S_2, \tag{2.2}$$

where the initial canonical orbital angular momentum $L_{\rm in}$ is related to $b_{\rm NR}$ and $P_{\rm ADM}$ by [106]

$$L_{\rm in} = 2X|P_y| = P_{\rm ADM} b_{\rm NR}. \tag{2.3}$$

We adopt as initial lapse profile $\alpha = \psi_{\rm BL}^{-2}$, where $\psi_{\rm BL}$ denotes the Brill-Lindquist conformal factor [7,111,113]. In Appendix A, we present a check that the uncertainty linked to the choice of initial lapse profile has a subdominant effect on the inferred scattering angle $\theta_{\rm NR}$ compared to the errors in the polynomial fits used to measure the scattering angle.

Time evolution is performed using the W-variant [114] of the BSSNOK formulation [115–117] of the Einstein field equations as implemented by the `McLachlan` [118] thorn. We evolve the BHs using moving punctures gauge conditions [7,119], the lapse is evolved using the $1 + \log$ condition [120], and the shift is evolved using the hyperbolic $\tilde{\Gamma}$-driver equation [113]. We use eighth-order accurate finite differencing stencils with Kreiss-Oliger dissipation [121]. Adaptive mesh refinement is provided by `Carpet`, with the near zone being computed with high-resolution Cartesian grids that track the motion of the BHs and the wave extraction zone being computed on spherical grids using the `Llama` multipatch infrastructure [122]. The apparent horizons are computed using `AHFinderDirect` [123] and the spin angular momenta are calculated using the dynamical horizon formalism provided by the `QuasiLocalMeasures` thorn [124].

Similarly to [106], we found that the total energy and angular momentum of the system left after the release of the burst of spurious radiation present in the initial data differ from the corresponding ADM quantities computed from the initial data only by negligible fractions of order 10^{-5}.

All ETK simulations were managed using `Simulation Factory` [125] and postprocessing of NR data has made

[1] As a check, we have also performed simulations with the same initial energy as [106].

[2] We do not compare here numerical scattering angles to state-of-the-art post-Newtonian predictions. Reference [106] made such comparisons in the nonspinning case and found that PN-expanded angles performed badly, compared to corresponding PN-based EOB-defined ones.

used of the open source Mathematica package SIMULATION TOOLS [126].

A. Extracting the scattering angle

In order to calculate the scattering angle, we follow the prescription detailed in [106]. The motion of the BHs is tracked by the Cartesian coordinates of the punctures in the center-of-mass frame. We convert the tracks to polar coordinates (r,φ) (in the x-y plane of motion) for each BH and treat the incoming $\varphi_{\mathrm{in},i}(r)$ and outgoing $\varphi_{\mathrm{out},i}(r)$ paths for the ith BH separately. We fit each of the paths to a polynomial of order n in terms of $u=1/r$ and extrapolate to find the asymptotic angle $\varphi^{\infty}_{\mathrm{in/out},i}$. The resulting scattering angle for the ith particle is given by

$$\theta_i = \varphi^{\infty}_{\mathrm{out},i} - \varphi^{\infty}_{\mathrm{in},i} - \pi. \tag{2.4}$$

Our choice of fitting window for (u,φ) follows [106], and we assume $r\in[14,80]M$ and $r\in[20,100]M$ for the incoming and outgoing trajectories respectively. We implement a least-squares fitting method that uses a singular value decomposition (SVD) to drop singular values smaller than 10^{-13} times the maximum singular value, as was used in [106]. In order to gauge the errors on the scattering angle, we perform a number of sanity checks. The first check is to gauge the impact of the polynomial order n on the resulting scattering angle. As in [106], the preferred polynomial order is taken to be the lowest order for which the SVD method allows for variation in the constant term. The extrapolation error is then estimated by finding the maximum and minimum scattering angle inferred over all polynomial orders between 2 and $n-1$. This generally leads to dissymmetric error bounds on the scattering angle: $\theta^{+\delta_+}_{-\delta_-}$. A value of 0 in δ_+ or δ_- occurs when the preferred polynomial is setting the bound. More precisely, $\delta_-=0$ (respectively $\delta_+=0$) occurs when the lower order polynomial fits over-estimate (respectively, under-estimate) the scattering angle relative to the preferred order. When least-square fitting our numerical results to analytical templates, we shall use a symmetrized version of the error bounds, namely $\pm\frac{1}{2}(\delta_++\delta_-)$.

Other sanity checks on the robustness of the derived scattering angle include testing the impact of the fitting window, testing the resolution of our numerical simulations, and varying gauge choices in the numerical evolution. We find that the inferred errors on the scattering angle remain subdominant to the choice of polynomial order, in agreement with the conclusions in [106]. See Appendix A for further details.

B. Nonspinning scattering simulations

Though the main aim of the present work is to simulate the scattering of spinning BBHs, we also performed systematic sequences of nonspinning simulations of BBHs with fixed initial energy and varying initial angular momenta in order to be able to extract direct numerical estimates of the EOB interaction potential (see Sec. V below). For the first sequence, we reproduced and extended the results of Ref. [106], with an initial (adimensionalized) ADM energy $\hat{E}^{\mathrm{ADM}}_{\mathrm{in}}\equiv E^{\mathrm{ADM}}_{\mathrm{in}}/M$ equal to $\hat{E}^{\mathrm{ADM}}_{\mathrm{in},1}\simeq 1.02264$ and varying initial (rescaled) orbital angular momentum $\hat{L}_{\mathrm{in}}\equiv L_{\mathrm{in}}/M^2$. This allowed us both to cross-check the accuracy of our computations and to probe more precisely the boundary between scattering and plunge. We also performed two more sequences at the higher incoming energies, $\hat{E}^{\mathrm{ADM}}_{\mathrm{in},2}\simeq 1.04033$ and $\hat{E}^{\mathrm{ADM}}_{\mathrm{in},3}\simeq 1.05548$. These explore a stronger-field region of the parameter space, with NR impact parameters going down to $\hat{b}_{\mathrm{NR}}\equiv b_{\mathrm{NR}}/M\simeq 6$ (with corresponding minimum isotropic EOB radial coordinate $\bar{r}^{\min}\simeq 2$, see below).

We report the results of all our nonspinning simulations in Table I. In Fig. 1 we show the scattering angles versus the impact parameter $\hat{b}_{\mathrm{NR}}$ for all three series of nonspinning systems. For the nonspinning simulations, we have that $\theta_{\mathrm{NR}}=\theta_1=\theta_2$.

TABLE I. Equal-mass, nonspinning NR simulations. The scattering angles have been replaced by dots where the black holes have plunged. An asterisk denotes simulations where there is uncertainty on an eventual plunge. Longer simulations are required to determine whether the system becomes bound after the first encounter.

$\hat{b}_{\mathrm{NR}}$	$\hat{E}^{\mathrm{ADM}}_{\mathrm{in}}$	$\hat{L}^{\mathrm{ADM}}_{\mathrm{in}}$	θ_{NR} [deg]
9.40	1.02264	1.07690	⋯
9.50	1.02264	1.08840	$376.275^{+0.026}_{-14.69}$*
9.55	1.02264	1.09410	$329.057^{+0.003}_{-1.534}$
9.56	1.02264	1.09520	$323.422^{+0.000}_{-1.914}$
9.57	1.02264	1.09640	$318.394^{+0.000}_{-1.575}$
9.58	1.02264	1.09750	$313.764^{+0.000}_{-1.331}$
9.60	1.02264	1.09980	$305.734^{+0.056}_{-0.694}$
9.70	1.02264	1.11130	$274.368^{+0.074}_{-0.016}$
9.90	1.02264	1.13420	$235.447^{+0.912}_{-0.003}$
10.00	1.02264	1.14560	$221.823^{+0.762}_{-0.002}$
10.20	1.02264	1.16860	$200.810^{+0.620}_{-0.004}$
10.40	1.02264	1.19150	$184.684^{+0.221}_{-0.002}$
11.00	1.02264	1.26020	$152.106^{+0.055}_{-0.446}$
12.00	1.02264	1.37480	$120.804^{+0.013}_{-0.307}$
13.00	1.02264	1.48930	$101.616^{+0.059}_{-0.002}$
14.00	1.02264	1.60390	$88.260^{+0.337}_{-0.002}$
15.00	1.02264	1.71850	$78.296^{+0.520}_{-0.002}$
16.00	1.02264	1.83300	$70.404^{+0.927}_{-0.003}$

(Table continued)

TABLE I. *(Continued)*

$\hat{b}_{\rm NR}$	$\hat{E}_{\rm in}^{\rm ADM}$	$\hat{L}_{\rm in}^{\rm ADM}$	$\theta_{\rm NR}$ [deg]
7.67	1.04032	1.15050	···
7.73	1.04032	1.15950	$392.815^{+0.006}_{-7.477}$*
7.77	1.04032	1.16550	$338.973^{+0.156}_{-0.756}$
7.80	1.04032	1.17000	$317.637^{+0.142}_{-0.444}$
7.87	1.04032	1.18050	$283.359^{+0.343}_{-0.007}$
7.93	1.04032	1.18950	$262.825^{+0.749}_{-0.008}$
8.00	1.04032	1.20000	$244.210^{+1.220}_{-0.005}$
8.40	1.04033	1.26000	$184.138^{+0.439}_{-0.004}$
8.80	1.04033	1.32000	$153.119^{+0.226}_{-0.227}$
9.00	1.04033	1.35000	$141.986^{+0.244}_{-0.213}$
9.40	1.04033	1.41000	$124.805^{+0.154}_{-0.238}$
9.50	1.04033	1.42500	$121.233^{+0.180}_{-0.153}$
9.60	1.04033	1.44000	$117.897^{+0.157}_{-0.091}$
10.00	1.04033	1.50000	$106.459^{+0.207}_{-0.004}$
12.00	1.04033	1.80000	$73.095^{+1.358}_{-0.006}$
14.00	1.04033	2.10000	$56.489^{+1.242}_{-0.006}$
16.00	1.04033	2.40000	$45.982^{+1.530}_{-0.008}$
6.00	1.05548	1.05000	···
7.00	1.05548	1.22500	$354.118^{+0.307}_{-0.633}$
7.20	1.05548	1.26000	$248.950^{+1.203}_{-0.005}$
7.40	1.05548	1.29500	$206.064^{+1.479}_{-0.006}$
7.60	1.05548	1.33000	$179.815^{+0.484}_{-0.006}$
8.00	1.05548	1.40000	$146.516^{+0.354}_{-0.096}$
9.00	1.05548	1.57500	$104.166^{+0.361}_{-0.006}$
10.00	1.05548	1.75000	$82.275^{+0.924}_{-0.007}$
11.00	1.05548	1.92500	$68.351^{+1.485}_{-0.007}$

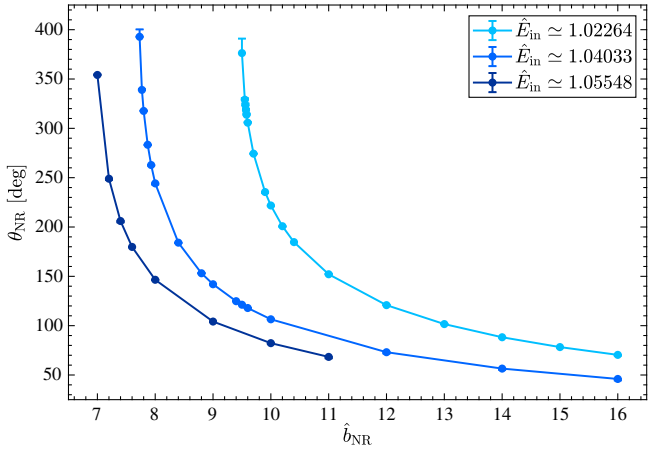

FIG. 1. NR scattering angles against impact parameter for the (equal-mass) nonspinning simulations. Higher-energy systems are able to probe stronger fields (smaller separations) without plunging.

C. Spinning scattering simulations

We present here the results of 35 NR simulations of hyperbolic encounters of (equal-mass) spinning BBHs. As far as we know, it is the first time unequal-spin simulations have been published. In particular, we compute a suite of simulations at fixed energy and (canonical) orbital angular momentum and various spin magnitudes. The main parameters of these simulations are reported in Table II, while the scattering angles, as a function of the rescaled spin variables χ_i are shown in Fig. 2.

When unequal spins are considered, the system ceases to be symmetric, inducing a nonzero recoil on the system center-of-mass. The effect of recoil on the scattering has been investigated in Ref. [86]. As a consequence of Eq. (3.33) there, the scattering angles measured using the individual trajectories of the two bodies will be different. In the following, we will denote by $\theta_{\rm NR}$ the relative scattering angle, which, for equal-mass binaries, is simply given (to linear order in the recoil) by

$$\theta_{\rm NR} = \frac{\theta_1 + \theta_2}{2}. \tag{2.5}$$

III. NR-DEDUCED PHYSICAL OBSERVABLES

In this section, we discuss some observables that can be directly extracted from the NR simulations presented in Sec. II above by using only minimal analytical assumptions.

A. Critical orbital angular momentum L_0 in nonspinning scattering

We define the critical (canonical) angular momentum L_0 of nonspinning binaries as the value marking the boundary between scattering and plunging systems. Several works (both analytical [58,127–130] and numerical [104,105,131–133]) have investigated the value of L_0 (and the subtleties in defining it in view of the importance of radiation losses).

Here we follow Ref. [133] in estimating L_0 by fitting the sequence of NR scattering angles at fixed energy using a template expected to capture the singular behavior of $\theta(L)$ as $L \to L_0^+$. Namely, we use (recalling the notation $\hat{L} \equiv L/M^2$)

$$\theta_{\rm NR}^{\rm fit}(\hat{L}) = \frac{\hat{L}}{\hat{L}_0} \ln\left(\frac{1}{1-\hat{L}_0/\hat{L}}\right)\left[\hat{\chi}_{\rm 3PM}(\hat{L};\hat{L}_0) + 2\frac{a_4}{\hat{L}^4}\right], \tag{3.1}$$

where $\hat{\chi}_{\rm 3PM}(\hat{L};\hat{L}_0)$ is a third order polynomial in $1/\hat{L}$ defined so as to ensure a correct PM expansion up to 3PM, and where a_4 is a 4PM-level fitting parameter (see Sec. VI A of Ref. [133] for details).

For the lower-energy simulations ($\hat{E}_1 = 1.02264$), we could improve the estimate of L_0 computed in Ref. [133] and get

TABLE II. NR equal-mass, spinning simulations with (approximately) fixed incoming energy $\hat{E}_{\rm in}^{\rm ADM} \simeq 1.02264$ and fixed orbital angular momentum $\hat{L}_{\rm in}^{\rm ADM} = 1.14560$. The columns, from left to right, represent the individual spins, the incoming (rescaled) ADM energy, the incoming (rescaled) orbital ADM angular momentum, the scattering angle of the two individual objects (replaced by dots when the objects plunge), and the average scattering angle $\theta_{\rm NR}$ with its two-sided uncertainty.

χ_1	χ_2	$\hat{E}_{\rm in}^{\rm ADM}$	θ_1 [deg]	θ_2 [deg]	$\theta_{\rm NR}$ [deg]
−0.30	−0.30	1.02269	...	...	...
−0.25	−0.25	1.02268	367.529	367.562	$367.545^{+0.000}_{-4.840}$*
−0.23	−0.23	1.02267	334.344	334.346	$334.345^{+0.084}_{-1.573}$
−0.22	−0.22	1.02267	322.693	322.693	$322.693^{+0.099}_{-1.004}$
−0.21	−0.21	1.02267	312.795	312.795	$312.795^{+0.187}_{-0.364}$
−0.20	−0.20	1.02266	303.910	303.858	$303.884^{+0.222}_{-0.466}$
−0.17	−0.17	1.02266	286.603	286.604	$286.603^{+0.154}_{-0.010}$
−0.16	−0.16	1.02266	277.848	277.850	$277.849^{+0.230}_{-0.003}$
−0.15	−0.15	1.02265	272.602	272.603	$272.603^{+0.260}_{-0.003}$
−0.10	−0.10	1.02265	251.027	251.029	$251.028^{+0.559}_{-0.003}$
−0.05	−0.05	1.02264	234.747	234.389	$234.568^{+0.845}_{-0.003}$
0.00	0.00	1.02264	221.822	221.823	$221.823^{+0.762}_{-0.002}$
0.05	0.05	1.02264	211.195	211.195	$211.195^{+0.610}_{-0.002}$
0.05	−0.05	1.02264	221.950	221.782	$221.866^{+0.643}_{-0.002}$
0.10	0.10	1.02265	202.763	202.453	$202.608^{+0.388}_{-0.002}$
0.15	0.15	1.02265	194.542	194.542	$194.542^{+0.183}_{-0.001}$
0.15	−0.15	1.02265	222.141	221.632	$221.887^{+0.637}_{-0.002}$
0.20	−0.20	1.02266	222.148	221.490	$221.819^{+0.863}_{-0.003}$
0.20	0.20	1.02266	187.839	187.838	$187.838^{+0.020}_{-0.141}$
0.30	0.30	1.02269	176.588	176.585	$176.586^{+0.001}_{-0.653}$
0.40	−0.40	1.02274	222.488	221.206	$221.847^{+0.849}_{-0.003}$
0.40	0.00	1.02269	188.456	187.819	$188.138^{+0.008}_{-0.132}$
0.40	0.40	1.02274	167.545	167.544	$167.545^{+0.002}_{-0.947}$
0.50	−0.30	1.02275	203.759	202.484	$203.121^{+0.477}_{-0.002}$
0.60	−0.60	1.02288	223.008	221.153	$222.080^{+0.808}_{-0.003}$
0.60	0.00	1.02276	178.087	177.170	$177.629^{+0.001}_{-0.645}$
0.60	0.60	1.02288	154.139	154.139	$154.139^{+0.005}_{-1.443}$
0.70	−0.30	1.02284	191.175	189.640	$190.407^{+0.013}_{-0.164}$
0.70	0.30	1.02284	161.186	160.685	$160.935^{+0.004}_{-1.274}$
0.80	−0.80	1.02309	222.855	220.504	$221.679^{+0.489}_{-0.002}$
0.80	−0.50	1.02294	199.960	198.026	$198.993^{+0.237}_{-0.001}$
0.80	0.00	1.02287	170.873	169.914	$170.394^{+0.003}_{-1.026}$
0.80	0.20	1.02288	162.421	161.716	$162.069^{+0.005}_{-1.308}$
0.80	0.50	1.02295	152.464	152.143	$152.303^{+0.006}_{-1.640}$
0.80	0.80	1.02309	145.467	145.248	$145.357^{+0.006}_{-1.528}$

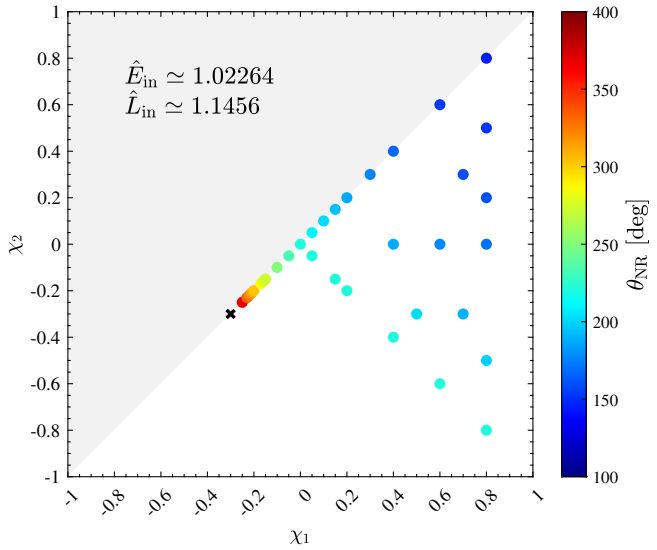

FIG. 2. NR scattering angles for equal-mass simulations with $\hat{E}_{\rm in} \simeq 1.02264$ and $\hat{L}_{\rm in} \simeq 1.1456$ against individual spin variables. This figure shows (see the color code) that the angles essentially depend only on the sum of the spins.

$$\hat{L}_0^{\rm fit}(\hat{E}_1) = 1.0787 \pm 0.00028,$$
$$a_4^{\rm fit}(\hat{E}_1) = 6.78 \pm 0.50. \tag{3.2}$$

The corresponding estimate of $\hat{L}_0^{\rm fit}(\hat{E}_1)$ in [133] is $\hat{L}_0^{\rm fit}(\hat{E}_1) = 1.0773$.

Instead, for the higher-energy ones ($\hat{E}_2 = 1.04033$ and $\hat{E}_3 = 1.05548$, respectively corresponding to center-of-mass velocities $v_{\rm cm,2} \simeq 0.2757$ and $v_{\rm cm,3} \simeq 0.3199$), we got

$$\hat{L}_0^{\rm fit}(\hat{E}_2) = 1.15305 \pm 0.00029,$$
$$a_4^{\rm fit}(\hat{E}_2) = 12.83 \pm 0.81, \tag{3.3}$$

and

$$\hat{L}_0^{\rm fit}(\hat{E}_3) = 1.21431 \pm 0.00036,$$
$$a_4^{\rm fit}(\hat{E}_3) = 20.2 \pm 1.8. \tag{3.4}$$

In Fig. 3 we display these numerical estimates against $v_{\rm cm}$. Note that the two new values $\hat{L}_0^{\rm fit}(\hat{E}_2)$ and $\hat{L}_0^{\rm fit}(\hat{E}_3)$ fill a gap in the previous knowledge of the critical $\hat{L}_0$ for intermediate energies. Figure 3 also displays the critical angular momentum estimates obtained through the high-velocity simulations of Refs. [104,105]. We compare these to analytical estimates based on using the EOB transcription of PM scattering results ($w^{\rm eob}$ nPM). For more details on these, see Sec. IV of Ref. [133].

We can also compare the fitted values $a_4^{\rm fit}(\hat{E}_n)$, $n = 1, 2, 3$, or more precisely the corresponding 4PM scattering coefficient, $\theta_4^{\rm fit}(\hat{E}_n)$, to the recently determined

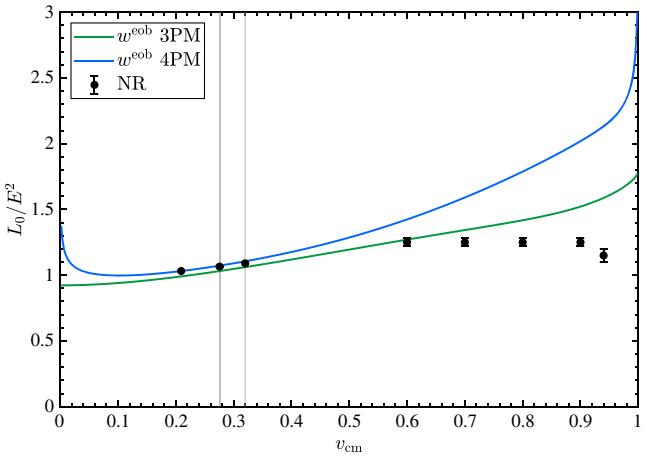

FIG. 3. Comparison between the critical (rescaled) orbital angular momentum L_0/E^2 extracted from NR simulations and various analytical predictions. The three leftmost NR data points correspond to our fitted estimates [Eqs. (3.2)–(3.4)]. The first point updates the estimate of Ref. [106], while the other two (highlighted by a vertical gray line) explore a new velocity interval. The five points on the right correspond to the high-energy simulations of Refs. [104,105]. We also display, for comparison, some EOB-PM predictions.

(radiation-reacted) analytical value of the function $\theta_4(\hat{E})$ [67,78,81,88]. We find $\theta_4^{\rm fit}(\hat{E}_1) \simeq 60.66$ [to be compared to $\theta_4^{\rm analyt}(\hat{E}_1) = 58.16$], as well as $\theta_4^{\rm fit}(\hat{E}_2) \simeq 84.93$ [to be compared to $\theta_4^{\rm analyt}(\hat{E}_2) = 77.07$] and $\theta_4^{\rm fit}(\hat{E}_3) \simeq 109.23$ [to be compared to $\theta_4^{\rm analyt}(\hat{E}_3) = 94.34$].

When considering spinning systems, the critical curve $L_0/E^2 = F(\hat{E})$ becomes a critical surface $L_0/E^2 = F(\hat{E},\chi_1,\chi_2)$. In the following subsection we show how to obtain one point on this critical surface.

B. Spin dependence of the scattering angle

We now focus on the spinning simulations and try to determine from our NR results (with minimal analytical assumptions) the spin dependence of the scattering angle at fixed initial energy and angular momentum. The color coding of Fig. 2 makes it apparent that the scattering angle mainly depends on the sum of the spins, i.e., is nearly constant along the lines $\chi_1 + \chi_2 = \text{const}$. In particular, the simulations with opposite spins ($\chi_1 = -\chi_2$, i.e., the second diagonal in Fig. 2) all lead to scattering angles $\theta_{\rm NR}$ very close (within the percent level) to the nonspinning one at the center. This numerical result corresponds to the well-known analytical fact (see, e.g., [134]) that the leading-PN value of the linear-in-spin interaction potential (spin-orbit) depends on the effective spin $\mathbf{S}_{\rm eff} = [1 + 3m_2/(4m_1)]\mathbf{S}_1 + [1 + 3m_1/(4m_2)]\mathbf{S}_2$, while the leading-PN value of the spin-spin interaction potential depends on $\mathbf{S}_0 = (1 + m_2/m_1)\mathbf{S}_1 + (1 + m_1/m_2)\mathbf{S}_2$. In the equal-mass case considered here, this means that the two leading-order spin-dependent interactions only depend on the total spin $\mathbf{S}_{\rm tot} = \mathbf{S}_1 + \mathbf{S}_2$, and therefore only on $\chi_1 + \chi_2$ in the spin-aligned case. We have found that this property remains true to a very good approximation, much beyond the leading-order PN approximation. As we will describe below, we have derived a high-PM-accuracy Hamiltonian incorporating the state of the art analytical knowledge of PM gravity, and we found (as displayed in Table V in Appendix C) that the averaged scattering angle of two (equal-mass) spinning BHs is analytically predicted to depend essentially only on the average spin $\chi_+ \equiv \frac{1}{2}(\chi_1 + \chi_2)$.

Let us also recall that the spin-orbit interaction term

$$H_{\rm SO} \simeq + \frac{2G}{c^3 r^3} \mathbf{L} \cdot \mathbf{S}_{\rm eff} \tag{3.5}$$

is repulsive (respectively, attractive) for spins parallel (respectively, antiparallel) to the orbital angular momentum $\mathbf{L}$. This fact has a strong effect on the last stable orbits of quasicircular spinning binaries (e.g., [134,135]). In the present, scattering situation, it implies that the leading-order spin-dependent contribution to the scattering angle is negative (positive) when $\mathbf{L} \cdot \mathbf{S}_{\rm eff} > 0$ ($\mathbf{L} \cdot \mathbf{S}_{\rm eff} < 0$), see e.g., [31]. This leading-order PN analytical prediction holds also true for the predictions from the PM-accurate EOB Hamiltonian derived below, as can be seen in the results displayed in Table VI in Appendix C.

Our numerical results (displayed in Fig. 2) agree remarkably well with the analytical expectation that the (average) scattering angle depends essentially on the average spin,

$$\chi_+ \equiv \frac{1}{2}(\chi_1 + \chi_2), \tag{3.6}$$

with only a weak dependence on the antisymmetric spin combination

$$\chi_- \equiv \frac{1}{2}(\chi_1 - \chi_2). \tag{3.7}$$

In particular, the numerical results displayed in Table II show that, for most of the (half) spin differences explored by our simulations, the dependence of $\theta_{\rm NR} \equiv \frac{1}{2}(\theta_1 + \theta_2)$ on χ_- stays within the numerical uncertainty with which we could determine $\theta_{\rm NR}$. For instance, even when $\chi_- = 0.80$, Table II reports that the difference between $\theta_{\rm NR}(\chi_1 = 0, \chi_2 = 0) = 221.823^{+0.762}_{-0.002}$ and $\theta_{\rm NR}(\chi_1 = 0.80, \chi_2 = -0.80 = 221.679^{+0.489}_{-0.002}$ is only 0.144 ± 0.454. In view of this finding, the present limited precision of our numerical results does not allow us to meaningfully extract any reliable estimate of the dependence of the function $\theta_{\rm NR}(\chi_+,\chi_-)$ on χ_-. [We note in passing that, for the equal-mass systems we are considering, the relative (i.e., average) scattering angle

$\theta_{\rm rel} = \frac{1}{2}(\theta_1 + \theta_2)$ is a symmetric function of χ_1 and χ_2, and therefore an even function of χ_-.]

On the other hand, if we focus (for maximum accuracy) on the equal-spin subset of our numerical results ($\chi_1 = \chi_2$, so that $\chi_+ = \chi_1 = \chi_2$, and $\chi_- = 0$), we can fit our results to various possible analytical templates so as to extract a numerical estimate of the univariate function $\theta_{\rm NR,eq}(\chi_+) = \theta_{\rm NR}(\chi_+, \chi_- = 0)$. Removing the $(\chi_1 = \chi_2 = -0.17)$ data point (which stood out as an outlier compared to its neighboring data points in all our fits; see also Fig. 6), we found that we could fit within numerical errors[3] the remaining 18 equal-spin data points to the following simple five-parameter template:

$$\theta^{\rm fit}_{\rm NR,eq}(\chi_+) = \frac{1 - \ln(\chi_+ - \chi_+^{\rm crit})}{1 - \ln(-\chi_+^{\rm crit})} \times (\theta_0 + \theta_1\chi_+ + \theta_2\chi_+^2 + \theta_3\chi_+^3). \tag{3.8}$$

Note that this template incorporates a logarithmic singularity at some critical spin $\chi_+^{\rm crit}$. This singularity models the image on the χ_+ axis of the logarithmic singularity generically expected when crossing the border between scattering and coalescence [133]. We find the best-fit values (when measuring angles in *radians*) to be

$$\begin{aligned} \theta_0 &= 3.8748 \pm 0.0017, \\ \theta_1 &= 1.881 \pm 0.018, \\ \theta_2 &= 0.43 \pm 0.10, \\ \theta_3 &= 1.07 \pm 0.13, \\ \chi_+^{\rm crit} &= -0.2932 \pm 0.0013, \end{aligned} \tag{3.9}$$

leading to a satisfactory reduced chi-squared: $\chi^2/(18-5) \simeq 0.63$.

The successful fit of our numerical results to the template (3.8) allows us to meaningfully extract from our NR results an estimate of the critical value of χ_+ (at least in the equal-spin case) leading to immediate plunge rather than scattering. Indeed, the value $\chi_+^{\rm crit} = -0.2932 \pm 0.0013$ formally corresponds to an infinite scattering angle. This result completes the critical values of L_0 displayed in Fig. 3 by yielding the numerical estimate of one point on the surface $L_0^{\rm crit}/E^2 = F(\hat{E}, \chi_1, \chi_2)$ describing the critical initial data for spinning BBHs leading to immediate coalescence, namely the point

$$L_0^{\rm crit}/E^2 = 1.0953, \quad \hat{E} = 1.02264, \quad \chi_1 = \chi_2 = -0.2932. \tag{3.10}$$

[3]Note that we are neglecting here the additional source of error linked to the fact that the initial energies of our simulations varies by $\pm O(10^{-3})$ from the averaged energy $E_{\rm in}^{\rm av} = 1.0227$.

The computations above have been based on the relative scattering angle $\theta_{\rm rel} = \frac{1}{2}(\theta_1 + \theta_2)$. We leave to future work a NR-based study of the dissymmetry between θ_1 and θ_2 linked to asymmetric-spin recoil effects.

IV. PM-BASED ANALYTICAL PREDICTIONS

In this section, we compare the NR data presented in Sec. II to analytical PM results for the scattering angle of a BBH system on hyperbolic orbits. For nonspinning BHs, these terms are known up to 4PM, including radiation-reaction effects [66,67,69,79,81,88]. The PM formalism has also been extended to include spinning objects, with PM accuracies depending on the order in spin [136–150].

A. Post-Minkowskian expanded scattering angles

In the nonspinning limit, the PM approximation (which is a power series in the gravitational constant G) translates to a power series in $1/\ell$, where ℓ denotes the rescaled orbital angular momentum,

$$\ell = \frac{L}{G\mu M}. \tag{4.1}$$

The total (nonspinning) scattering angle up to nPM order (included) can then be written as

$$\theta^{\rm orb}_{n\rm PM}(\gamma, \ell) \equiv \sum_{k=1}^{n} 2\frac{\theta_k^{\rm orb}(\gamma)}{\ell^k}, \tag{4.2}$$

where γ denotes the Lorentz factor between the two incoming worldlines. We recall that γ is equal to the rescaled EOB effective energy, $\gamma = E_{\rm eff}^{\rm eob}/\mu$, which is related to the (real) total energy of the system by

$$\gamma = \frac{E^2 - m_1^2 - m_2^2}{2m_1 m_2}. \tag{4.3}$$

When considering spinning BHs, the PM expansion is modified because of the spin-induced multipolar structure of BHs. More precisely, the multipolar structure of Kerr BHs is polynomial in the Kerr parameters $a_i = S_i/m_i$ (with dimension of length), so that each spin-order, $O(S^m)$ involves a mth order polynomial in a_1 and a_2. In the current PM literature on spinning bodies, it is usual to consider the Kerr parameters (or "ring radii") a_i, as expansion parameters independent of the basic PM expansion parameters Gm_1, Gm_2. In other words, one uses a double expansion in powers of Gm_i (PM expansion), and in powers of a_i (spin expansion). This leads to a double counting (n, m), in which the PM order n counts the (sum of the) powers of Gm_i, while m counts the (sum of the) powers of a_i. However, one must remember that we are interested in the dynamics of spinning BH's for which we have the inequality $a_i \leq Gm_i$. Therefore, a term

of order $(Gm)^n a^m$ is of real PM order $n+m$. This issue must be kept in mind, and will come back in our discussion below, but, for compatibility with the literature, we will continue to refer to a term of order $(Gm)^n a^m$ as being formally of n-PM order.

The natural dimensionless expansion parameters associated with the PM and spin expansions are Gm_i/b and a_i/b where b denotes the impact parameter. We will, instead of b, use the (rescaled) angular momentum $\ell \equiv L/(Gm_1m_2)$, with $L = P_{\rm cm} b$. We also utilize $S_i = m_i a_i$ as spin variables, so that each spin order will be identified by a corresponding power of S_i/ℓ. One then writes the combined PM, and spin, expansion of the scattering angle as (in the spin-aligned case)

$$\theta_{n\rm PM}(\gamma, \ell, S_i) \equiv \sum_{k=1}^{n} 2 \frac{\theta_k(\gamma, \ell, S_i)}{\ell^k}, \tag{4.4}$$

with the kPM contribution to the scattering angle, $\theta_k(\gamma, \ell, S_i)$, being further expanded in spin powers, namely

$$\theta_k(\gamma, \ell, S_i) \equiv \sum_{m \geq 0} \frac{\theta_k^{\rm S^m}(\gamma)}{\ell^m}. \tag{4.5}$$

Here, $\theta_k^{\rm S^m}(\gamma)$ denotes a homogeneous polynomial in the two spins of order m. For instance

$$\theta_k^{\rm S}(\gamma) = \theta_k^{\rm S_1}(\gamma) S_1 + \theta_k^{\rm S_2}(\gamma) S_2, \tag{4.6}$$

$$\theta_k^{\rm S^2}(\gamma) = \theta_k^{\rm S_1^2}(\gamma) S_1^2 + \theta_k^{\rm S_1 S_2}(\gamma) S_1 S_2 + \theta_k^{\rm S_2^2}(\gamma) S_2^2. \tag{4.7}$$

As several theoretical papers on spinning scattering use as basic variables covariantly defined impact parameters, spins and orbital angular momentum (say $L_{\rm cov}$), while we work here with the canonically defined orbital angular momentum ($L \equiv L_{\rm can}$), we need to recall the connection between $L_{\rm cov}$ and $L \equiv L_{\rm can}$. In the spin-aligned case, it is simply given by using the relation [138]

$$J = L_{\rm can} + m_1 a_1 + m_2 a_2 = L_{\rm cov} + E_1 a_1 + E_2 a_2, \tag{4.8}$$

where $a_i = S_i/m_i$ and $E_i = \sqrt{m_i^2 + P_{\rm c.m.}^2}$. In order to obtain the coefficients $\theta_k^{\rm S^m}$ of the double PM- and spin-expansion as functions of the canonical orbital angular momentum, we transform $L_{\rm cov}$ into $L_{\rm can}$ using Eq. (4.8), reexpand in powers of spin, and neglect higher-order contributions.

In the following, when considering spinning systems, we include: (i) nonspinning contributions up to 4PM (including radiation-reaction effects) [65,66,69,81,86,87]; (ii) quadratic-in-spin terms up to the 3PM order (including radiation-reaction effects) [145]; (iii) cubic and fourth order in spin effects up to the 2PM order [60]. In addition, as during the development of this work the conservative [151], and radiative [152], linear-in-spin contributions have been computed at the 4PM level, we also incorporated these new analytical results. Their impact is separately discussed below.

B. $w^{\rm eob}$ resummed scattering angles

In addition to PM-expanded scattering angles, we also compute $w^{\rm eob}$-resummed PM angles, as introduced in Ref. [133] and generalized here to spinning bodies.

Let us briefly introduce the EOB formalism (see, e.g., Sec. II B of Ref. [133] for more details). The EOB framework [17,18,153] is a way of mapping the general-relativistic dynamics of two masses m_1, m_2 (considered in the center-of-mass system) onto the effective relativistic dynamics of a single body of mass $\mu = m_1 m_2/(m_1+m_2) = \nu M$. The "real" center-of-mass Hamiltonian is related to the "effective" one through

$$H_{\rm real} = M \sqrt{1 + 2\nu \left(\frac{H_{\rm eff}}{\mu} - 1 \right)}. \tag{4.9}$$

For scattering motions, the value of the effective energy $E_{\rm eff} = H_{\rm eff}$ is simply related to the Lorentz factor $\gamma = -u_1 \cdot u_2$ between the two incoming worldlines by $E_{\rm eff} = \mu\gamma$. This implies that the total ADM energy of the system is related to γ via

$$\hat{E} = \frac{E}{M} = \sqrt{1 + 2\nu(\gamma - 1)}. \tag{4.10}$$

The effective Hamiltonian $H_{\rm eff}$ is obtained by solving (in $P_0 = -H_{\rm eff}$) some relativisticlike mass-shell condition of the general form

$$0 = \mu^2 + g_{\rm eff}^{\mu\nu} P_\mu P_\nu, + Q(R, P_\mu), \tag{4.11}$$

where $Q(R, P_\mu)$ gathers terms more than quadratic in P_μ. When considering scattering problems, it is convenient to use a mass-shell condition where the effective metric is the Schwarzschild metric, and where $Q(R, P_\mu)$ is expressed as a function of the effective energy $-P_0 = \mu\gamma$. Using isotropic coordinates, and rescaled variables, $\bar{r} = R/M$, $p_\alpha = P_\alpha/\mu$, the PM-expansion of the EOB mass-shell condition formally takes the form of a nonrelativistic energy-conservation law, namely [58,154]

$$p_{\bar{r}}^2 + \frac{\ell^2}{\bar{r}^2} = p_\infty^2 + w^{\rm eob}(\bar{r}; \gamma), \tag{4.12}$$

where $p_\infty = \sqrt{\gamma^2 - 1}$ and where the Newtonian-looking potential $w^{\rm eob}(\bar{r}; \gamma)$ [more precisely, $-w^{\rm eob}(\bar{r})$] encapsulates the (relativistic, energy-dependent) attractive gravitational

interaction. For nonspinning systems, the PM expansion of the $w^{\rm eob}$ potential reads

$$w^{\rm orb}_{n\rm PM}(\bar{r},\gamma)=\sum_{k=1}^{n}\frac{w^{\rm orb}_k(\gamma)}{\bar{r}^k}, \tag{4.13}$$

where each order in $\frac{1}{\bar{r}}$ corresponds to the same PM order (e.g., the first term, $\frac{w^{\rm orb}_1(\gamma)}{\bar{r}}$, with $w^{\rm orb}_1(\gamma)=2(2\gamma^2-1)$, describes the 1PM gravitational interaction [57]).

For aligned-spin binaries we can generalize Eq. (4.13) simply by considering a spin-dependent radial potential of the form (up to fourth order in the spins)

$$w_{n\rm PM}(\bar{r},\gamma,\ell,S_i)=w^{\rm orb}(\bar{r},\gamma)+\frac{\ell w^{\rm S}_{n\rm PM}(\bar{r},\gamma)}{\bar{r}^2}+\frac{w^{\rm S^2}_{n\rm PM}(\bar{r},\gamma)}{\bar{r}^2}+\frac{\ell w^{\rm S^3}_{n\rm PM}(\bar{r},\gamma)}{\bar{r}^4}+\frac{w^{\rm S^4}_{n\rm PM}(\bar{r},\gamma)}{\bar{r}^4}. \tag{4.14}$$

Here each $w^{\rm S^m}_{n\rm PM}(\bar{r},\gamma)$ is a polynomial of order m in spins, whose coefficients admit an expansion in powers of $\frac{1}{\bar{r}}$ up to the order $\frac{1}{\bar{r}^n}$ included. For instance, we have (at spin orders $m=1$ and $m=2$)

$$w^{\rm S}_{n\rm PM}(\bar{r},\gamma)=\sum_{k=1}^{n}\frac{w^{\rm S_1}_k(\gamma)S_1+w^{\rm S_2}_k(\gamma)S_2}{\bar{r}^k}, \tag{4.15}$$

$$w^{\rm S^2}_{n\rm PM}(\bar{r},\gamma)=\sum_{k=1}^{n}\frac{w^{\rm S_1^2}_k(\gamma)S_1^2+w^{\rm S_1S_2}_k(\gamma)S_1S_2+w^{\rm S_2^2}_k(\gamma)S_2^2}{\bar{r}^k}. \tag{4.16}$$

The energy-dependent $w^*_k(\gamma)$ coefficients entering the EOB potentials are in 1-to-1 correspondence with the $\theta^*_k(\gamma)$ coefficients of the scattering angle expansion. These relations can be found by expanding, and solving, at each order in G and in spin, the following equation:

$$\pi+\theta(\gamma,\ell,S_i)=-2\int_{\bar{r}_{\rm min}}^{+\infty}d\bar{r}\frac{\partial p_{\bar{r}}(\bar{r},\gamma,\ell,S_i)}{\partial\ell}=\int_{\bar{r}_{\rm min}}^{+\infty}\frac{d\bar{r}}{\bar{r}^2}\frac{2\ell-w^{\rm S}(\bar{r},\gamma)-w^{\rm S^3}(\bar{r},\gamma)/\bar{r}^2}{\sqrt{p_\infty^2-\ell^2/\bar{r}^2+w(\bar{r},\gamma,\ell,\chi_i)}}. \tag{4.17}$$

Here $\bar{r}_{\rm min}$ denotes the turning point radius. The explicit equations linking the $\theta^*_k(\gamma)$ coefficients and the $w^*_k(\gamma)$ ones are given in Appendix B. When using the existing PM-expanded results for the scattering angle, the relations of Appendix B allow one to compute the explicit values of the PM-expansion coefficients $w^*_k(\gamma)$ describing the spin interactions within the EOB formalism. These values will be found in the ancillary file of this paper [155]. Note that the so-constructed EOB potential is a function of the incoming energy and angular momentum of the system that incorporates both conservative and radiation-reaction effects.

Following Ref. [133], we then define spin-dependent $w^{\rm eob}$-resummed scattering angles $\theta^{w}_{n\rm PM}(\gamma,\ell,S_i)$ by substituting the nPM-accurate, spin-dependent, EOB potentials $w_{n\rm PM}(\bar{r},\gamma,\ell,S_i)$ in Eq. (4.17), without performing any expansion (in G or in spin), i.e.,

$$\pi+\theta^{w^{\rm eob}}_{n\rm PM}\equiv\int_0^{\bar{u}_{\rm max}}d\bar{u}\frac{2\ell-w^{\rm S}_{n\rm PM}-w^{\rm S^3}_{n\rm PM}\bar{u}^2}{\sqrt{p_\infty^2-\ell^2\bar{u}^2+w_{n\rm PM}}}, \tag{4.18}$$

where we introduced $\bar{u}\equiv 1/\bar{r}$ and $\bar{u}_{\rm max}=1/\bar{r}_{\rm min}$.

V. COMPARING NUMERICAL RESULTS TO ANALYTICAL PREDICTIONS

A. Numerics/analytics comparison for nonspinning simulations

We start by comparing, in Fig. 4, the results of the nonspinning NR simulations at fixed energy to both the PM-expanded, perturbative, predictions, Eq. (4.4), and their EOB-resummed versions, defined by Eq. (4.18). This comparison extends the one considered in Refs. [95,133], which corresponded to the lower initial energy $\hat{E}_1$ used in [106] (see also Appendix C). The main findings of the latter comparison when considering the PM-expanded perturbative predictions remain true for the new, higher energies considered in this paper, $\hat{E}_2=1.04033$ and $\hat{E}_3=1.05548$. The sequence of PM-expanded results (dashed lines) monotonically approach, in an increasingly accurate way, the NR results in the high angular momenta domain (i.e., for relatively large impact parameters fields). However, they perform less and less well as the angular momentum decreases. Note, in particular, that, for our minimum $\hat{L}$, even the 4PM-accurate prediction differs by a factor $\gtrsim 2$ from the NR result.

On the other hand, the sequence of $w^{\rm eob}$-resummed (PM-based) predicted angles (solid lines) perform much better than their perturbative counterparts. While the 1PM-based $w^{\rm eob}$-resummed prediction is not better (and even slightly worse) than its perturbative analog, the 2PM-based $w^{\rm eob}$-resummed fares as well as the 4PM perturbative one, and the 3PM and, especially, 4PM EOB-resummed results exhibit a remarkable agreement with NR data for essentially all orbital angular momenta. It should, however, be noted that the 4PM-based EOB-resummed predicted angles start to show visible discrepancies with NR results for the lowest L's, especially for the highest energy $\hat{E}_3=1.05548$. More precisely, $w^{\rm eob}_{4\rm PM}$ somewhat overestimates the scattering angle, while $w^{\rm eob}_{3\rm PM}$ underestimates it. We discuss below how these findings can lead to NR-based ways of improving the knowledge of the exact $w^{\rm eob}(\bar{r},\gamma)$ potential.

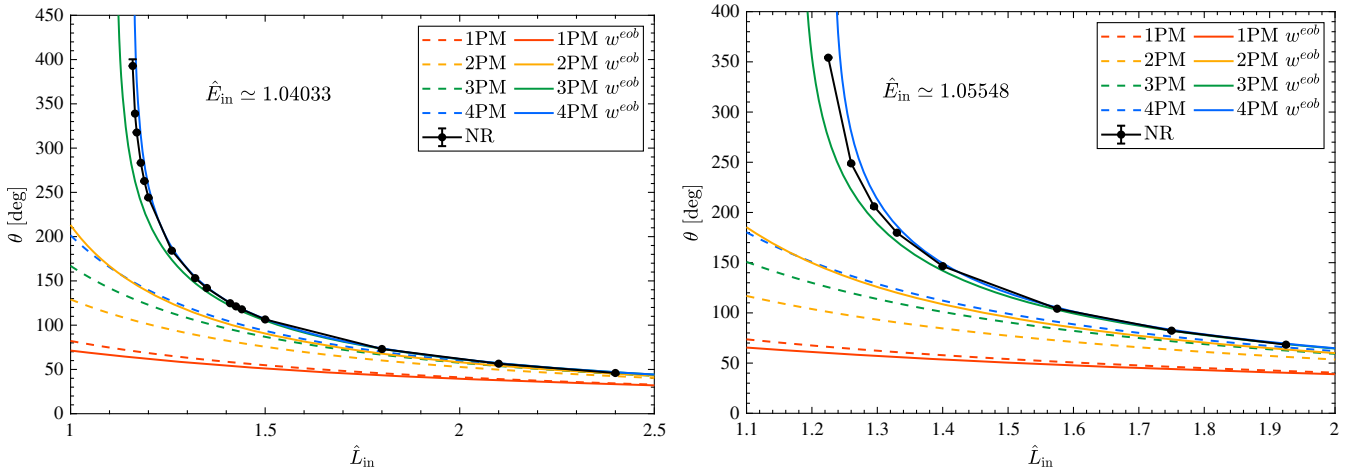

FIG. 4. Comparison between NR scattering angles of nonspinning BBH systems and analytical PM predictions, both PM-expanded (dashed lines) and $w^{\rm eob}$-resummed (solid lines). Left panel: Intermediate energy $\hat{E}_{\rm in} \simeq 1.04033$. Right panel: Higher energy $\hat{E}_{\rm in} \simeq 1.05548$. The $w^{\rm eob}$-resummed 3PM and 4PM results show a remarkable agreement with numerical down to strong-field regimes.

B. Extracting from NR results the gravitational interaction potential between nonspinning black holes

Having computed new suites of numerical simulations with higher initial energies, we can extend the strategy used in Sec. VI C of Ref. [133] and directly extract from the sequence of NR scattering angles (at a given energy) the NR radial potential $w_{\rm NR}(\bar{r})$ (in our chosen EOB coordinates). This extraction is done by iteratively using Firsov's inversion formula [156,157] to invert the functional relation $w(\bar{r},\gamma) \to \theta(\ell,\gamma)$, Eq. (4.17) (for nonspinning systems), i.e. to deduce the function $w_{\rm NR}(\bar{r})$ leading to the function $\theta_{\rm NR}(\ell)$, tabulated in Table I (for each fixed value of γ).

The so-extracted NR radial potential for the lower value $\gamma_1(E_1) \simeq 1.09188$ has been displayed in Fig. 7 of Ref. [133]. See Appendix C for an updated determination of $w_{\rm NR}(\bar{r},\gamma_1)$. We focus here on the determination of the NR potentials $w_{\rm NR}(\bar{r},\gamma_2)$ and $w_{\rm NR}(\bar{r},\gamma_3)$ corresponding to the two higher-energy sequences of simulations reported in the present work. In addition, we compare the so-extracted NR gravitational potentials to their analytical counterparts, as defined by the PM-based EOB radial potential $w^{\rm eob}(\bar{r},\gamma)$ defined in Eq. (4.13) above (for the nonspinning case).

Instead of plotting the various energy-dependent radial potentials $w^*(\bar{r},\gamma)$, it is useful to plot the corresponding "effective radial potentials", completed by the additional centrifugal potential $+\frac{\ell^2}{\bar{r}^2}$. In other words, we shall compare the (Newtonian-like) effective potentials

$$V^*(\bar{r},\gamma,\ell) \equiv \frac{\ell^2}{\bar{r}^2} - w^*(\bar{r},\gamma), \tag{5.1}$$

made by adding the (repulsive) centrifugal barrier term $\ell^2\bar{r}^{-2}$ to the (attractive) gravitational radial potential $-w^*(\bar{r},\gamma)$.

The comparison between $V^{\rm NR}(\bar{r},\gamma,\ell)$ and $V^{\rm eob}_{n{\rm PM}}(\bar{r},\gamma,\ell)$ (for $n=3$ and $n=4$) is displayed in the two panels of Fig. 5. The left panel corresponds to the intermediate energy $\gamma_2(E_2) \simeq 1.16456$, and uses the smallest NR orbital angular momentum leading to scattering, namely $\hat{L} \simeq 1.15950$ (corresponding to $\hat{b}_{\rm NR} = 7.73$). The right panel corresponds to the higher energy $\gamma_3(E_3) \simeq 1.22808$, and uses the smallest NR orbital angular momentum leading to scattering for that energy, namely $\hat{L} \simeq 1.22500$ (corresponding to $\hat{b}_{\rm NR} = 7.00$). The NR-extracted potentials are determined only for (isotropic) radii larger than about 1.95 (for E_2) and about 1.85 (for E_3).

Note that, for both energies, the NR-extracted potential is very close to the 4PM-based EOB potential down to radii $\bar{r} \simeq 2.8$. However, in the interval $2 \lesssim \bar{r} \lesssim 2.8$ $V^{\rm eob}_{\rm 4PM}(\bar{r})$ starts to exhibit visible differences with $V^{\rm NR}(\bar{r})$. For the intermediate energy E_2 the peak of $V^{\rm eob}_{\rm 4PM}$ lies just below the p^2_∞ line, meaning that the EOB-4PM potential predicts a plunge instead of a scattering for this angular momentum and this energy. By contrast, the (less attractive) EOB-3PM potential still predicts scattering for this angular momentum and this energy. The situation is similar for the highest energy, E_3. In this case, the NR potential seems to interpolate between $V^{\rm eob}_{\rm 4PM}(\bar{r})$ and $V^{\rm eob}_{\rm 3PM}(\bar{r})$.

These results suggest that it would be useful to resum the EOB-PM potentials,[4] so as to improve their performances

[4]We recall that we use here PM-expanded EOB radial potentials $w(\bar{r}) \sim \frac{1}{\bar{r}} + \frac{1}{\bar{r}^2} + \frac{1}{\bar{r}^3} + \cdots$.

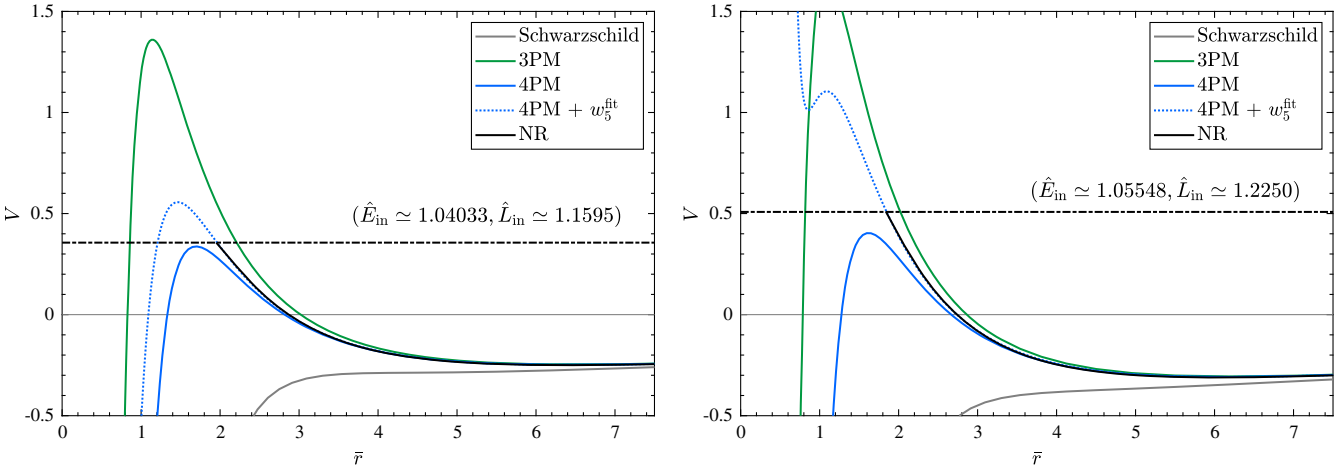

FIG. 5. Comparison between the gravitational potential V extracted from NR simulations and its EOB-PM equivalent. The Schwarzschild potential is plotted as a reference. Left panel: Intermediate energy $\hat{E}_{\rm in} \simeq 1.04033$. Right panel: Higher energy $\hat{E}_{\rm in} \simeq 1.05548$. In both cases, the angular momentum is set to the smallest values of angular momentum for which the system scattered. The horizontal lines mark the values of p_∞^2 for each energy, determining the maximum point up to which it is possible to extract information about the numerical potential.

at small radii. Leaving such an investigation to future work, we shall content ourselves here by exploring the effect of adding a formal, additional 5PM-level contribution $+\frac{w_5(\gamma)}{\bar{r}^5}$ to the analytically predicted 4PM EOB potential. We can use our determination of $w^{\rm NR}(\bar{r})$ to extract a best-fit value for the (energy-dependent) coefficient $w_5(\gamma)$. Fitting (for our three energies) $w^{\rm NR}(\bar{r},\gamma)$ to $w^{\rm eob}_{\rm 4PM}(\bar{r}) + \frac{w_5(\gamma)}{\bar{r}^5}$ yields the following results:

$$
\begin{aligned}
w_5^{\rm fit}(\gamma_1) &= -1.00 \pm 0.17, \\
w_5^{\rm fit}(\gamma_2) &= -2.16 \pm 0.13, \\
w_5^{\rm fit}(\gamma_3) &= -3.47 \pm 0.23.
\end{aligned} \tag{5.2}
$$

Here the errors are indicative estimates obtained by applying the parametric inversion formulas to the confidence intervals defined by Eqs (3.2)–(3.4).

The negative sign (present at all energies) reflects the fact that the EOB-4PM potential is slightly too attractive at small radii (while the EOB-3PM potential is too repulsive for all radii). The strange behaviour of $V^{\rm fit}(\bar{r}) = V^{\rm eob}_{\rm 4PM}(\bar{r}) - \frac{w_5^{\rm fit}(\gamma)}{\bar{r}^5}$ at small radii, for the highest energy (right panel of Fig. 5) indicates that the addition of a (repulsive) 5PM term is only physically valid in a small range of radii (say in the range $2 \lesssim \bar{r} \lesssim 2.8$). Indeed, when one uses a nonresummed potential, $w(\bar{r}) = \frac{w_1}{\bar{r}} + \frac{w_2}{\bar{r}^2} + \cdots \frac{w_n}{\bar{r}^n}$, the last term determines the strong-field behavior. In particular, a negative 5PM term entails a (probably unphysical) repulsive core at very small radii. The use of suitably resummed versions of the EOB-PM potentials would probably avoid such undesirable features.

C. Comparing spinning simulations to analytical predictions (without 4PM spin-orbit terms)

We now shift our attention to the suite of 35 NR simulations which computed the scattering angles of systems having many different spins, but with fixed initial energy ($\hat{E}_{\rm in} \simeq 1.02264$) and orbital angular momentum ($\hat{L}_{\rm in} = 1.14560$). As we have already seen in Sec. III that the scattering angle mainly depends on the average spin χ_+, we actually focus on the 19 simulations with equal spins (varying between $\chi_1 = \chi_2 = -0.30$ and $\chi_1 = \chi_2 = +0.80$) listed in Table II.

In Fig. 6, we compare the equal-mass, equal-spin simulations to two types of PM-informed predictions: (i) standard PM-expanded angles, of the type of Eq. (4.4); and (ii) $w^{\rm eob}$-resummed ones [see Eq. (4.18)]. In this section, we do not take into account the recently derived linear-in-spin (spin-orbit) 4PM results of Refs. [151,152]. In other words, we only use at the 4PM level (conservative and radiative) orbital effects. Since the analytical PM knowledge of the spin-dependent couplings varies with the spin order, we shall consider, for simplicity, only the following cases: (i) 1PM accuracy in all couplings up to quartic-in-spin terms (labelled as 1PM); (ii) 2PM accuracy in all couplings up to S^4 (labeled as 2PM); (iii) 3PM accuracy in the (S^0, S^1, S^2) couplings and 2PM accuracy in the (S^3, S^4) ones (labeled as 3PM); and (iv) respectively (4PM,3PM,3PM,2PM,2PM) accuracy in the $(S^0, S^1, S^2, S^3, S^4)$ couplings (labeled as 4PM).

A first conclusion one can draw from Fig. 6 is that PM-expanded results are rather unsatisfactory. Both the spin-averaged baseline and the spin-dependence are inaccurate, even for the highest PM accuracy. The agreement becomes, however, more satisfactory in the high-positive-spin

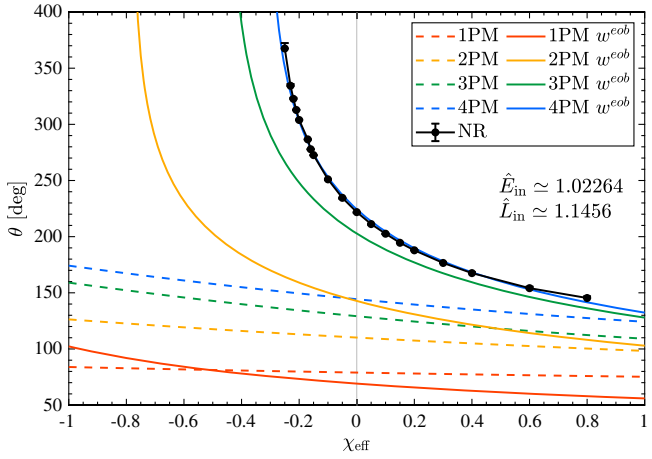

FIG. 6. Scattering angle comparison between NR data and both the perturbative, and the EOB-transcribed, PM-based predictions for equal-mass, equal-spin simulations. The x-axis represents $\chi_{\rm eff} = \chi_1 = \chi_2$. As in Fig. 4, we use dashed lines for the PM-expanded scattering angles, while the solid lines correspond to the $w^{\rm eob}$-resummed ones. Similarly to the nonspinning case, the $w^{\rm eob}$-resummed predictions are markedly more accurate, especially the 4PM-informed ones.

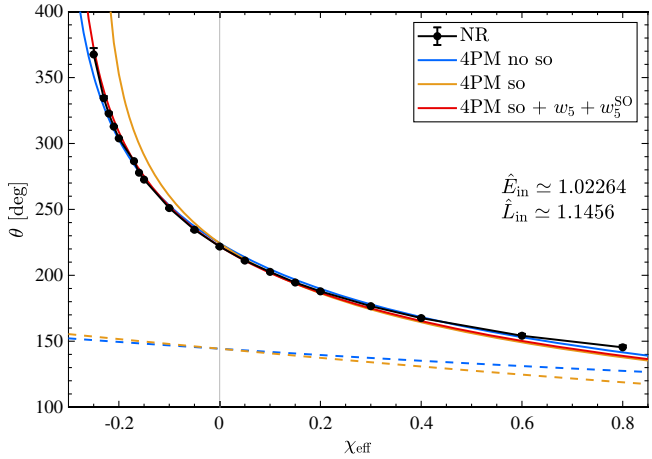

FIG. 7. Effects due to the inclusion of the 4PM spin-orbit contributions [151,152] to the scattering angle comparison of Fig. 6. Dashed lines correspond to PM-expanded scattering angles, while solid lines represent $w^{\rm eob}$-resummed predictions. The blue curves contain spin-dependent terms up to 3PM and nonspinning contributions at 4PM (as in Fig. 6 above). The orange curves also incorporate (radiation-reacted) spin-orbit effects at 4PM level. Finally, the red line includes the two additional parameters w_5 and $w_5^{\rm SO}$ of Eqs. (5.3) and (5.4).

domain, which involves (because of the repulsive effect of parallel spins) weaker-field interactions.

By contrast, the $w^{\rm eob}$-resummed angles show, at each PM order, a systematically better agreement with NR data points, especially for the 4PM accuracy which exhibits a remarkable agreement.

D. Inclusion of 4PM spin-orbit terms

As already mentioned, conservative and radiative 4PM-level linear-in-spin contributions have been computed [151,152] during the development of this work. We transformed the latter scattering-angle results into additional contributions to the 4PM EOB potential $w^{\rm S}_{\rm 4PM}$.

In Fig. 7 we compare the effect of incorporating the radiatively corrected 4PM spin-orbit terms ("4PM so"), to the 4PM-level angles computed in the previous section which only included orbital effects at 4PM ("4PM no so"). For simplicity, we do not separately consider here the conservative contribution to the 4PM spin-orbit terms.

Though the inclusion of 4PM spin-orbit terms has a relatively minor effect in the PM-expanded scattering angles (see dashed lines), their inclusion in $w^{\rm S}_{\rm 4PM}$ leads to much larger differences with respect to the corresponding 4PM-level EOB-resummed angles displayed in Fig. 6.

Looking at Fig. 7, it is clear that PM-expanded results remain rather unsatisfactory, and are significantly less accurate than $w^{\rm eob}$-resummed ones. However, the inclusion of 4PM-level spin-orbit effects in $w^{\rm eob}$ worsens the EOB-NR agreement that was obtained when only including 4PM-level orbital coefficients.

It is possible that the worsening due to the inclusion of 4PM spin-orbit terms is a signal pointing out the need to introduce some resummation of the spin-dependent $w^{\rm S}_{\rm eob}$ potential. [We recall that we are using here PM-expanded $w^{\rm S}_{\rm eob}$ potentials, as indicated in Eq. (4.14).] However, the main cause of the worsening effect of the inclusion of 4PM spin-orbit terms might be the fact, recalled in Sec. IV above, that the nomenclature used in current spin-dependent PM works is physically inappropriate when dealing with spinning BHs. Indeed, because of the Kerr BH limit $a_i \leq Gm_i$, a term of formal n-PM order including the mth power of spins is actually of $(n+m)$-PM order. Therefore, the additional spin-orbit contributions computed in [151,152] are actually at the physical 5PM order. Similarly, the formally 2PM-level terms quartic in spins [140] are actually at the physical 6PM order.

In view of the latter remark, we have explored the effect of including an additional spin-dependent term in $w^{\rm eob}$ belonging to the formal 5PM level, but to the physical 6PM level. For simplicity, we only considered a term involving a linear-in-spin contribution of the form

$$\Delta w^{\rm eob} = \frac{w_5}{\bar{r}^5} + \frac{w_5^{\rm SO} \ell \chi_{\rm eff}}{\bar{r}^7}. \tag{5.3}$$

This additional term contains two dimensionless parameters: (i) w_5, parametrizing an orbital 5PM-level contribution; and

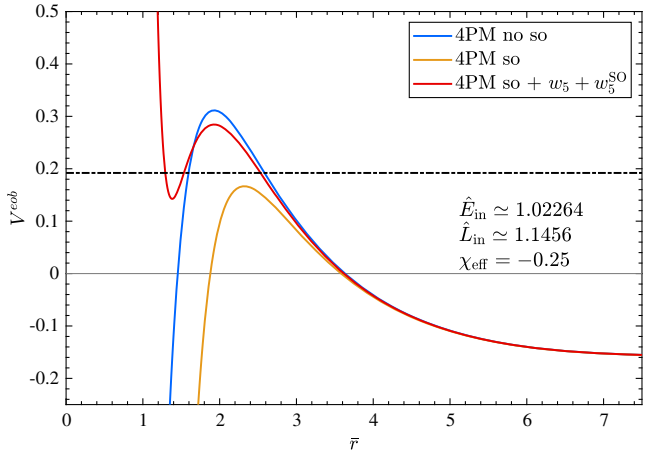

FIG. 8. Comparison of various EOB-PM gravitational potentials V^{eob} in the most negative spin case ($\chi_{eff} = -0.25$), i.e., the leftmost NR point in previous figures. The displayed analytical potentials correspond to the solid lines in Fig. 7. The horizontal line marks the "energy level" p_∞^2 defining the turning point of the EOB mass-shell condition, Eq. (4.12).

(ii) w_5^{SO}, parametrizing a spin-orbit contribution at the physical 6PM level.[5]

In view of our above finding that the purely orbital part of the EOB potential is slightly too attractive and needs to be completed by a $\frac{w_5(\gamma)}{\bar{r}^5}$ term, where $w_5(\gamma)$ is an energy-dependent negative coefficient, we fix its value to $w_5^{fit}(\gamma_1)$, Eq. (5.2), as the incoming energy of our spinning simulations corresponds to $\hat{E}_1 \equiv \hat{E}(\gamma_1)$. Concerning the second, spin-orbit-related, parameter w_5^{SO} in Eq. (5.3), we determine it by imposing that the corresponding effective Newtonian-like potential V^{eob}, Eq. (5.1), predicts immediate coalescence for the critical value $\chi_{crit} = -0.2932 \pm 0.0013$, Eq. (3.9), obtained above by fitting numerical results to the simple template of Eq. (3.8). This fixes the two parameters entering Eq. (5.3) to the approximate values

$$w_5 = -1.00 \pm 0.17,$$
$$w_5^{SO} = +17.3 \pm 0.6. \tag{5.4}$$

The corresponding w^{eob}-resummed scattering angles computed using the (central) values of Eq. (5.4) are displayed in Fig. 7 as a red curve (labelled "4PM so $+ w_5 + w_5^{SO}$"). The addition of the term Δw^{eob}, Eq. (5.3), leads to a better visual agreement between NR and EOB, at least for negative spins (on the large positive spin side, it slightly worsens the NR-EOB difference).

In order to better understand the physical origin of the differences between the various 4PM-level curves displayed in Fig. 7, we plot in Fig. 8 the corresponding Newtonian-like effective potentials V^{eob}, Eq. (5.1). Let us recall the meaning of the labels in Fig. 7: (i) "4PM no so" refers to a potential including (radiation-reacted) 4PM orbital effects without including any spin-orbit contributions at 4PM; (ii) "4PM so" additionally includes 4PM radiatively-corrected spin-orbit terms [152]; and finally (iii) "4PM so $+ w_5 + w_5^{SO}$" differs from "4PM so" by including the potential Δw^{eob}, Eq. (5.3), with the (central) values of Eq. (5.4). The dash-dotted horizontal line corresponds to the value of p_∞^2, which defines the turning point of the EOB mass-shell condition, Eq. (4.12).

The vertical distance between "4PM no so" (blue line) and "4PM so" (orange line) measures the effect of the (radiation-reacted) 4PM spin-orbit contribution. The inclusion of these terms leads to a more attractive potential. Actually, the corresponding potential is now below the p_∞^2 "energy level" which means that the system is predicted to no longer scatter but to plunge (in agreement in Fig. 7).

The Δw^{eob} correction makes the potential (red line) more repulsive. This leads to a turning point around $\bar{r} \simeq 2.5$ and to a finite scattering angle. This corrected potential also includes a (probably unphysical) repulsive core around $\bar{r} \simeq 1$.

At this stage, the meaning of these results is unclear. One will need to explore more values of the incoming energy, of the incoming angular momentum, and of the spins to assess whether it is indeed necessary to add (energy-dependent) terms, such as Eq. (5.3), to the current best analytical knowledge of the EOB potential.

VI. DISCUSSION

In this paper we presented numerical simulations of the scattering of equal-mass BBHs using the EINSTEIN TOOLKIT [109].

We first computed three sequences of equal-mass, nonspinning BBHs at fixed initial energy and varying angular momentum. The first sequence, with initial energy $\hat{E}_{in,1} \simeq 1.02264$, reproduces and extends the results of Ref. [106]. These served as a useful cross-check against previous simulations performed with different numerical codes. They were also used to improve the estimate of the critical angular momentum L_0, marking the boundary between scattering and plunging systems. We then computed two other sequences of simulations at higher energies, $\hat{E}_{in,2} \simeq 1.04033$ and $\hat{E}_{in,3} \simeq 1.05548$, probing stronger-field regimes. These two series allowed us to compute the critical angular momentum L_0 in previously unexplored regions of center-of-mass velocities, $v_{cm,2} \simeq 0.2757$ and $v_{cm,3} \simeq 0.3199$. This leaves as regions not yet covered by NR simulations of nonspinning BHs the low velocity regime, $v_{cm} \lesssim 0.2$, and the intermediate velocity one, $v_{cm} \simeq 0.3$–0.6.

We then presented, for the first time, a suite of numerical simulations of equal-mass aligned-spins BHs. For these,

[5]For simplicity, we do not include here a purely orbital 6PM-level contribution $w_6/\bar{r}^6$.

we fixed both initial energy and angular momentum to be $(\hat{E}_{\rm in}, \hat{L}_{\rm in}) \simeq (1.02264, 1.1456)$ and varied the individual spins in the range $-0.3 < \chi_i < 0.8$. We found (as expected both from NR simulations of coalescing binaries and from analytical predictions) the spin interaction to depend mainly on the total spin. We extracted from numerical data the coefficients of the linear and quadratic spin dependence of the scattering angle at the considered energy and angular momentum.

We compared our numerical results to PM-based predictions for the scattering angles of equal-mass BHs. We used two types of PM-based analytical predictions: (i) usual, perturbative PM-expanded results, see Eq. (4.4); and (ii) a transcription of PM results within the EOB formalism using a (spin-dependent, radiation-reacted) radial potential in isotropic (EOB) gauge, $w^{\rm eob}(\bar{r}, L, S_1, S_2)$, see Eq. (4.18). We found that PM-expanded scattering angles exhibit (both for nonspinning and spinning systems) an acceptable agreement with NR data only for large impact parameters, consistently with the PM framework being a weak-field expansion. On the contrary, a transcription of the PM information into a corresponding (energy-dependent, radiation-reacted, spin-dependent) EOB gravitational potential $w^{\rm eob}(\bar{r}, L, S_1, S_2)$ yields remarkable improvements in the scattering angle comparisons, especially when using the highest available PM accuracy. See Figs. 4 and 6. In the case of spinning simulations, we found that the inclusion of the recently computed 4PM-level spin-orbit contribution worsened the remarkable agreement (displayed in Fig. 6) between NR angles and the EOB-resummed 4PM-level ones (without 4PM spin-orbit terms). See Fig. 7.

Visible discrepancies between NR results and EOB-PM-predicted ones occur only for the few nonspinning cases where the impact parameter is close to the critical one leading to plunge rather than scattering and, for spinning simulations, when including the 4PM-level spin-orbit contributions. See Fig. 5, where we compare (for nonspinning systems) the EOB-PM potential to a corresponding potential directly extracted from the NR scattering data by inverting the relation: potential → scattering angle. We could, however, improve the accuracy of the EOB-PM gravitational potential by adding (an NR-fitted) additional (energy-dependent) 5PM-level contribution $w_5^{\rm fit}(\gamma)/\bar{r}^5$, see Eq. (5.2). Similarly, in the spinning case, we could improve the NR-EOB match obtained when incorporating the 4PM-level radiation-reacted spin-orbit terms by including an additional (formally) 5PM-level contribution including a spin-orbit term, Eqs. (5.3) and (5.4). The sensitivity of the dynamics to spin-dependent contributions at the 4PM level is studied in Fig. 8.

The present work can be extended in several directions. On the numerical side, a more thorough exploration of the parameter space is called for, notably by considering different energies, mass ratios, and spin orientations. In addition, it would be useful to complete the computation of the scattering angles by accurately estimating the emitted waveform, and by numerically estimating the corresponding radiative losses of energy, linear momentum and angular momentum.

On the analytical side, one should explore possible resummations of the EOB-PM radial potential, and generalize it to the nonaligned-spin case. It would also be interesting to explore other possible EOB reformulations of perturbative PM results, e.g., using different EOB gauges. Finally, when having in hands NR waveforms, one should compare them to the recent analytical computations of $O(G^3)$-accurate, PM-expanded waveforms [158–160].

Despite the above-mentioned limitations, we hope that the results presented here will offer a useful starting point for constructing accurate waveform models for spinning BHs in eccentric and hyperbolic motions, by combining information from NR and PM data within an EOB framework.

ACKNOWLEDGMENTS

The authors thank R. Russo for useful discussions during the development of this work. P. R. acknowledges the hospitality and the stimulating environment of the Institut des Hautes Etudes Scientifiques. The present research was partly supported by the *"2021 Balzan Prize for Gravitation: Physical and Astrophysical Aspects"*, awarded to Thibault Damour. P. R. acknowledges support by the Fondazione Della Riccia, A. A. 2021/2022. P. R. is supported by the Italian Minister of University and Research (MUR) via the PRIN 2020KB33TP, *Multimessenger astronomy in the Einstein Telescope Era (METE)*. L. M. T. is supported by STFC, the School of Physics and Astronomy at the University of Birmingham, and the Birmingham Institute for Gravitational Wave Astronomy. G. P. is very grateful for support from a Royal Society University Research Fellowship URF\R1\221500 and RF\ERE\221015, and gratefully acknowledges support from an NVIDIA Academic Hardware Grant. G. P. and P. S. acknowledge support from STFC Grant No. ST/V005677/1. Computations were performed using the University of Birmingham's BlueBEAR HPC service, which provides a High Performance Computing service to the University's research community, the Sulis Tier 2 HPC platform hosted by the Scientific Computing Research Technology Platform at the University of Warwick funded by EPSRC Grant No. EP/T022108/1 and the HPC Midlands + consortium, and on the Bondi HPC cluster at the Birmingham Institute for Gravitational Wave Astronomy.

APPENDIX A: NUMERICAL RELATIVITY SYSTEMATICS

1. Impact of NR resolution

One aspect of our numerical setup that can affect accuracy is the spatial resolution of the simulations. In order to test the robustness of the scattering angle to

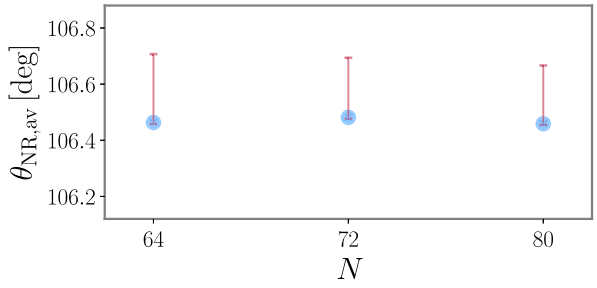

FIG. 9. Error on the average scattering angle $\theta_{\rm NR,av}$ derived from the numerical relativity simulations for three different resolutions on the finest grid. Here, $N = 80$ represents the highest resolution, and default choice, whereas $N = 64$ denotes the lowest resolution. For all three resolutions, the upper errors are set by lower-order polynomial fits that overestimate the scattering angle. The lower error bars are set by high-order polynomials that manifestly agree with the preferred order.

the NR resolution, we choose a fiducial binary and repeat the scattering simulation at three different resolutions, $N = [64, 72, 80]$. Here N denotes the number of grid points on the finest level such that the resolution of the smallest box around the puncture is $\sim 2m_p/N$, with $N = 64$ denoting the lowest resolution and $N = 80$ the highest. Here we take a nonspinning configuration with $P_{\rm ADM} = 0.15$ and $b_{\rm NR} = 10.0$. As shown in Fig. 9, we find that the choice of resolution has a minimal impact on the scattering angle, with the errors due to finite NR resolution being subdominant to the errors from the polynomial extrapolation. A summary is given in Table III.

2. Impact of gauge conditions

In order to help understand the impact of gauge conditions on our calculation of the scattering angle, we rerun a canonical test simulation, taken to be $b_{\rm NR} = 10.0$ and $\boldsymbol{P}_{\rm ADM} = 0.11456439$, with an alternative lapse profile. The default lapse profile, as noted in earlier, is $\alpha = \psi_{\rm BL}^{-2}$. For the alternative prescription, we adopt the lapse profile proposed in [161], which makes use of an approximate helical Killing vector field to minimize the dynamical evolution of the lapse. Writing the lapse in a precollapsed form, we have [161]

$$\tilde{\alpha} = \frac{1 - \left(\frac{m_1}{2r_1} + \frac{m_2}{2r_2}\right)}{1 + \frac{m_1}{2r_1} + \frac{m_2}{2r_2}}, \tag{A1}$$

TABLE III. A set of equal-mass, nonspinning simulations with an initial momentum $P_{\rm ADM} = 0.175$ and different resolutions.

N	$\hat{b}_{\rm NR}$	$\hat{E}_{\rm in}^{\rm ADM}$	$\hat{L}_{\rm in}^{\rm ADM}$	$\theta_{\rm NR}$[deg]
64	10.00	1.04033	1.50000	$106.463^{+0.243}_{-0.005}$
72	10.00	1.04033	1.50000	$106.481^{+0.212}_{-0.005}$
80	10.00	1.04033	1.50000	$106.459^{+0.207}_{-0.004}$

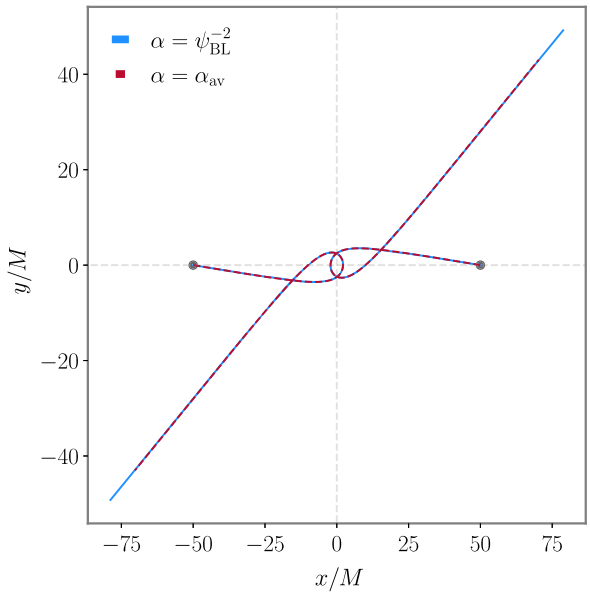

FIG. 10. Trajectories of each BH using two different gauge choices for the initial lapse. The first choice is $\alpha = \psi_{\rm BL}^{-2}$, and the second the averaged lapse defined in Eq. (A1). The dots denote the starting position of each BH.

where m_i and r_i denote the mass and location of the ith puncture respectively. The lapse is then averaged, $\alpha = (1 + \tilde{\alpha})/2$, to ensure that it lies within a range of [0, 1]. The initial shift is taken to be $\beta = 0$.

For this robustness test, we adopt a nonspinning, equal mass binary with $P_{\rm ADM} = 0.11456439$ and $b_{\rm NR}$, as shown in Fig. 10. We find that the choice of lapse again has a minor impact on the calculated scattering angle, finding $\theta_{\rm NR,av} = 221.823^{+0.762}_{-0.002}$ for the default lapse and $\theta_{\rm NR,av} = 222.089^{+0.605}_{-0.002}$ for the alternative lapse. The differences are smaller than the errors arising from the polynomial fitting procedure.

APPENDIX B: MAPPING BETWEEN SCATTERING ANGLE AND POTENTIAL COEFFICIENTS

We here report the relations between the w_i coefficients entering the radial potential $w_{n\rm PM}$, Eq. (4.14), and the θ_i coefficients constituting the scattering angle $\theta_{n\rm PM}$, Eq. (4.4).

We start by recalling the equations linking the various energy variables to the γ factor of the system,

$$\hat{E}_{\rm eff}^{\rm eob} \equiv \frac{E_{\rm eff}^{\rm eob}}{\mu} = \gamma,$$
$$\hat{E} \equiv \frac{E}{M} = \sqrt{1 + 2\nu(\gamma - 1)}. \tag{B1}$$

The relations between the nonspinning coefficients are known, and read

$$\theta_1^{\rm orb} = \frac{w_1^{\rm orb}}{2p_\infty},$$
$$\theta_2^{\rm orb} = \frac{\pi}{4} w_2^{\rm orb},$$
$$\theta_3^{\rm orb} = \frac{1}{p_\infty^3}\left[p_\infty^4 w_3^{\rm orb} + \frac{1}{2} p_\infty^2 w_2^{\rm orb} w_1^{\rm orb} - (w_1^{\rm orb})^3\right],$$
$$\theta_4^{\rm orb} = \frac{3\pi}{8}\left[p_\infty^2 w_4^{\rm orb} + w_3^{\rm orb} w_1^{\rm orb} + \frac{1}{2}(w_2^{\rm orb})^2\right]. \tag{B2}$$

In the following, we list the relations containing spin terms relevant to this paper; linear relations up to 4PM, quadratic-in-spin up to 3PM, cubic and quartic-in-spin at 1PM and 2PM. At linear order in spins we get

$$\theta_1^{\rm S} = \frac{p_\infty}{2} w_1^{\rm S},$$
$$\theta_2^{\rm S} = \frac{\pi}{4}(p_\infty^2 w_2^{\rm S} + w_1^{\rm orb} w_1^{\rm S}),$$
$$\theta_3^{\rm S} = \frac{1}{p_\infty}\left[p_\infty^4 w_3^{\rm S} + \frac{3}{2} p_\infty^2 (w_2^{\rm orb} w_1^{\rm S} + w_1^{\rm orb} w_2^{\rm S}) + \frac{3}{8}(w_1^{\rm orb})^2 w_1^{\rm S}\right],$$
$$\theta_4^{\rm S} = \frac{3\pi}{8}\left[p_\infty^4 w_4^{\rm S} + 2p_\infty^2 (w_2^{\rm orb} w_2^{\rm S} + w_3^{\rm orb} w_1^{\rm S} + w_1^{\rm orb} w_3^{\rm S}) + (w_1^{\rm orb})^2 w_2^{\rm S} + 2w_2^{\rm orb} w_1^{\rm orb} w_1^{\rm S}\right], \tag{B3}$$

while the quadratic-in-spin terms read

$$\theta_1^{\rm S^2} = p_\infty w1,$$
$$\theta_2^{\rm S^2} = \frac{3\pi}{32}\left[3p_\infty^2 (w_1^{\rm S})^2 + 4p_\infty^2 w_2^{\rm S^2} + 4w_1^{\rm orb} w_1^{\rm S^2}\right],$$
$$\theta_3^{\rm S^2} = \frac{1}{p_\infty}\left\{\frac{4}{3} p_\infty^4 (w_3^{\rm S^2} + 2w_2^{\rm S} w_1^{\rm S}) + \frac{1}{2}(w_1^{\rm orb})^2 w_1^{\rm S^2} + 2p_\infty^2\left[w_2^{\rm orb} w_1^{\rm S^2} + w_1^{\rm orb}(w_1^{\rm S})^2 + w_1^{\rm orb} w_2^{\rm S^2}\right]\right\}. \tag{B4}$$

The cubic-in-spin and quadratic-in-spin contributions at 1PM order are simply

$$\theta_1^{\rm S^3} = p_\infty^3 w_1^{\rm S^3},$$
$$\theta_1^{\rm S^4} = \frac{4}{3} p_\infty^3 w_1^{\rm S^4}, \tag{B5}$$

while the 2PM coefficients can be obtained by

$$\theta_2^{\rm S^3} = \frac{3\pi}{8} p_\infty^2 \left(p_\infty^2 w_2^{\rm S^3} + 2w_1^{\rm orb} w_1^{\rm S^3} + 2w_1^{\rm S} w_1^{\rm S^2}\right),$$
$$\theta_2^{\rm S^4} = \frac{15\pi}{64} p_\infty^2 \left[2p_\infty^2 w_2^{\rm S^4} + 5p_\infty^2 w_1^{\rm S} w_1^{\rm S^3} + 4w_1^{\rm orb} w_1^{\rm S^4} + 2(w_1^{S_2})^2\right]. \tag{B6}$$

The explicit values of the w_i coefficients are given in the ancillary file of this paper [155].

APPENDIX C: ADDITIONAL POST-MINKOWSKIAN DATA POINTS

In this appendix, we complement the PM results presented in the main paper.

In Figs. 11 and 12, we mimic Figs. 4 and 5 for the nonspinning systems with lower energy, $\hat{E}_{\rm in,1} \simeq 1.02264$.

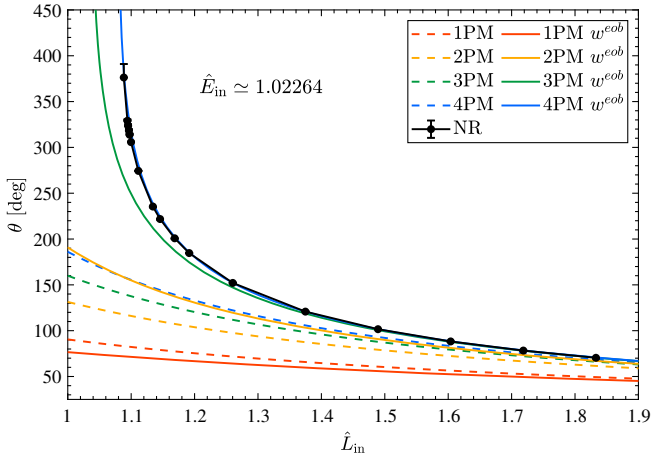

FIG. 11. Scattering angles against initial angular momentum (as in Fig. 4) for the lower-energy simulations of equal-mass nonspinning BBHs.

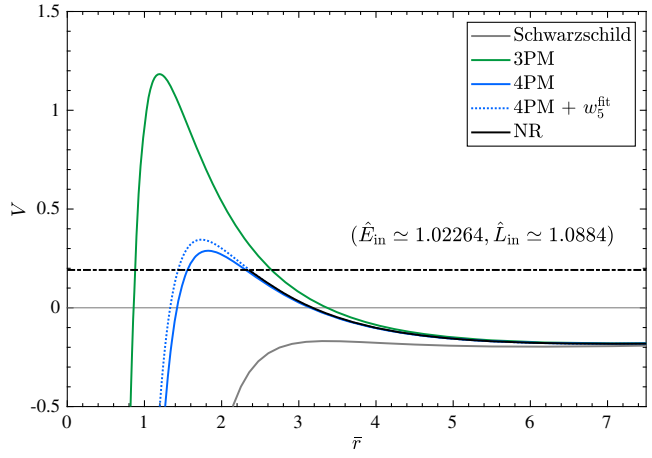

FIG. 12. Gravitational potential V as a function of (center-of-mass, isotropic coordinates) separation (as in Fig. 5) for the lower energy simulations of equal-mass nonspinning BBHs.

TABLE IV. NR equal-mass, nonspinning simulations presented in Table I. The last two columns list the $w^{\rm eob}$-resummed scattering angles at 3PM and 4PM as in Figs. 4 and 11. An asterisk denotes simulations where there is uncertainty on an eventual plunge. The scattering angles are replaced by dots when the BHs (are predicted to) plunge.

$\hat{E}_{\rm in}^{\rm ADM}$	$\hat{L}_{\rm in}^{\rm ADM}$	$\theta_{\rm NR}$ [deg]	$\theta^{w}_{\rm 3PM}$ [deg]	$\theta^{w}_{\rm 4PM}$ [deg]
1.02264	1.0769	⋯	288.979	⋯
1.02264	1.0884	$376.275^{+0.026}_{-14.69}$*	266.491	379.310
1.02264	1.0941	$329.057^{+0.003}_{-1.534}$	257.257	341.135
1.02264	1.0952	$323.422^{+0.000}_{-1.914}$	255.589	335.476
1.02264	1.0964	$318.394^{+0.000}_{-1.575}$	253.808	329.728
1.02264	1.0975	$313.764^{+0.000}_{-1.331}$	252.209	324.803
1.02264	1.0998	$305.734^{+0.056}_{-0.694}$	248.965	315.401
1.02264	1.1113	$274.368^{+0.074}_{-0.016}$	234.475	280.337
1.02264	1.1342	$235.447^{+0.912}_{-0.003}$	211.830	238.507
1.02264	1.1456	$221.823^{+0.762}_{-0.002}$	202.691	224.179
1.02264	1.1686	$200.810^{+0.620}_{-0.004}$	187.190	201.991
1.02264	1.1915	$184.684^{+0.221}_{-0.002}$	174.595	185.411
1.02264	1.2602	$152.106^{+0.055}_{-0.446}$	147.085	152.231
1.02264	1.3748	$120.804^{+0.013}_{-0.307}$	118.731	120.821
1.02264	1.4893	$101.616^{+0.059}_{-0.002}$	100.654	101.704
1.02264	1.6039	$88.260^{+0.337}_{-0.002}$	87.828	88.423
1.02264	1.7185	$78.296^{+0.520}_{-0.002}$	78.150	78.515
1.02264	1.833	$70.404^{+0.927}_{-0.003}$	70.539	70.777
1.04032	1.1505	⋯	295.902	⋯
1.04032	1.1595	$392.815^{+0.006}_{-7.477}$*	274.866	⋯
1.04032	1.1655	$338.973^{+0.156}_{-0.756}$	263.305	430.914
1.04032	1.17	$317.637^{+0.142}_{-0.444}$	255.591	374.716
1.04032	1.1805	$283.359^{+0.343}_{-0.007}$	240.035	312.437
1.04032	1.1895	$262.825^{+0.749}_{-0.008}$	228.777	282.302
1.04032	1.2	$244.210^{+1.220}_{-0.005}$	217.439	257.740
1.04033	1.26	$184.138^{+0.439}_{-0.004}$	173.732	187.734
1.04033	1.32	$153.119^{+0.226}_{-0.227}$	147.539	154.603
1.04033	1.35	$141.986^{+0.244}_{-0.213}$	137.744	143.094
1.04033	1.41	$124.805^{+0.154}_{-0.238}$	122.169	125.487
1.04033	1.425	$121.233^{+0.180}_{-0.153}$	118.900	121.880
1.04033	1.44	$117.897^{+0.157}_{-0.091}$	115.828	118.517
1.04033	1.5	$106.459^{+0.207}_{-0.004}$	105.174	107.016
1.04033	1.8	$73.095^{+1.358}_{-0.006}$	73.374	73.826
1.04033	2.1	$56.489^{+1.242}_{-0.006}$	56.993	57.160
1.04033	2.4	$45.982^{+1.530}_{-0.008}$	46.791	46.868
1.05548	1.05	⋯	⋯	⋯
1.05548	1.225	$354.118^{+0.307}_{-0.633}$	274.582	391.281
1.05548	1.26	$248.950^{+1.203}_{-0.005}$	222.675	280.445
1.05548	1.295	$206.064^{+1.479}_{-0.006}$	192.055	218.732
1.05548	1.33	$179.815^{+0.484}_{-0.006}$	170.787	186.552
1.05548	1.4	$146.516^{+0.354}_{-0.096}$	142.049	149.418
1.05548	1.575	$104.166^{+0.361}_{-0.006}$	103.162	105.287
1.05548	1.75	$82.275^{+0.924}_{-0.007}$	82.292	83.191
1.05548	1.925	$68.351^{+1.485}_{-0.007}$	68.882	69.339

TABLE V. NR equal-mass, spinning simulations listed in Table II. All systems were computed with fixed initial ADM energy $\hat{E}_{\rm in}^{\rm ADM} \simeq 1.02264$ and orbital ADM angular momentum $\hat{L}_{\rm in}^{\rm ADM} \simeq 1.14560$. The last two columns list the $w^{\rm eob}$-resummed scattering angles at 3PM and 4PM as in Fig. 6.

χ_1	χ_2	$\theta_{\rm NR}$ [deg]	$\theta^{w}_{\rm 3PM}$ [deg]	$\theta^{w}_{\rm 4PM}$ [deg]
−0.3	−0.3	⋯	209.786	494.626
−0.25	−0.25	$367.545^{+0.000}_{-4.840}$*	266.889	351.203
−0.23	−0.23	$334.345^{+0.084}_{-1.573}$	266.305	327.892
−0.22	−0.22	$322.693^{+0.099}_{-1.004}$	258.352	318.528
−0.21	−0.21	$312.795^{+0.187}_{-0.364}$	251.257	310.189
−0.2	−0.2	$303.884^{+0.222}_{-0.466}$	247.895	302.522
−0.17	−0.17	$286.603^{+0.154}_{-0.010}$	238.849	283.736
−0.16	−0.16	$277.849^{+0.230}_{-0.003}$	236.080	278.413
−0.15	−0.15	$272.603^{+0.260}_{-0.003}$	233.369	273.354
−0.1	−0.1	$251.028^{+0.559}_{-0.003}$	221.462	252.778
−0.05	−0.05	$234.568^{+0.845}_{-0.003}$	211.364	236.915
0.00	0.00	$221.823^{+0.762}_{-0.002}$	202.691	224.179
0.05	0.05	$211.195^{+0.610}_{-0.002}$	195.096	213.564
0.05	−0.05	$221.866^{+0.643}_{-0.002}$	202.986	224.175
0.10	0.10	$202.608^{+0.388}_{-0.002}$	188.382	204.533
0.15	0.15	$194.542^{+0.183}_{-0.001}$	182.347	196.652
0.15	−0.15	$221.887^{+0.637}_{-0.002}$	202.691	224.186
0.20	−0.2	$221.819^{+0.863}_{-0.003}$	202.698	224.201
0.20	0.20	$187.838^{+0.020}_{-0.141}$	176.910	189.726
0.30	0.30	$176.586^{+0.001}_{-0.653}$	167434	177.997
0.40	−0.4	$221.847^{+0.849}_{-0.003}$	202.771	224.357
0.40	0.00	$188.138^{+0.008}_{-0.132}$	1776.927	189.759
0.40	0.40	$167.545^{+0.002}_{-0.947}$	159.411	168.358
0.50	−0.3	$203.121^{+0.477}_{-0.002}$	188.440	204.657
0.60	−0.6	$222.080^{+0.808}_{-0.003}$	202.912	224.646
0.60	0.00	$177.629^{+0.001}_{-0.645}$	167.462	178.053
0.60	0.60	$154.139^{+0.005}_{-1.443}$	146.410	153.206
0.70	−0.3	$190.407^{+0.013}_{-0.164}$	177.005	189.915
0.70	0.30	$160.935^{+0.004}_{-1.274}$	152.489	160.234
0.80	−0.8	$221.679^{+0.489}_{-0.002}$	203.145	225.114
0.80	−0.5	$198.993^{+0.237}_{-0.001}$	182.518	196.996
0.80	0.00	$170.394^{+0.003}_{-1.026}$	159.445	168.433
0.80	0.20	$162.069^{+0.005}_{-1.308}$	152.494	160.249
0.80	0.50	$152.303^{+0.006}_{-1.640}$	143.642	150.049
0.80	0.80	$145.357^{+0.006}_{-1.528}$	136.199	141.643

These figures confirm the outstanding agreement between EOB-PM predictions and NR results found in Ref. [106].

In Tables IV and Tables V, we list the scattering angles for the presented NR simulations together with the

corresponding best-performing analytical predictions (not considering 4PM spin-orbit terms), $\theta^{w}_{\rm 3PM}$ and $\theta^{w}_{\rm 4PM}$.

Finally, we compare the spin dependence of the NR scattering angles to PM predictions in the small spin range. Using the simplifying fact that we are considering equal-mass systems, and the relative scattering angle $\theta_{\rm rel} = \frac{1}{2}(\theta_1 + \theta_2)$, we can write, at quadratic order in spins, the simple general template

$$\theta_{\rm rel}(\gamma, j; \chi_i) \overset{(m_1=m_2)}{=} \theta_0(\gamma, j) + \theta_{\chi_+}(\gamma, j)\chi_+ + \theta_{\chi_+^2}(\gamma, j)\chi_+^2 + \theta_{\chi_-^2}(\gamma, j)\chi_-^2 + \mathcal{O}[\chi^3]. \tag{C1}$$

We can, in principle, determine the θ_i coefficients for the initial energy and angular momentum of our simulations, $(\hat{E}_{\rm in}, \hat{L}_{\rm in}) \simeq (1.02264, 1.1456)$ by fitting the scattering angles for configurations with small (absolute) values of the spins. We decided to focus on the 6 configurations with $|\chi_{1/2}| \leq 0.1$ and to fit them to the template Eq. (C1) (truncated to quadratic terms). We so obtained the following values:

$$\begin{aligned} \theta_0^{\rm fit} &= 3.872 \pm 0.048, \\ \theta_{\chi_+}^{\rm fit} &= -4.211 \pm 0.031, \\ \theta_{\chi_+^2}^{\rm fit} &= 8.75 \pm 0.60, \\ \theta_{\chi_-^2}^{\rm fit} &= 0.6 \pm 3.1. \end{aligned} \tag{C2}$$

The reduced chi-squared of this fit is $\chi^2/(6-4) \simeq 1.17$ (corresponding to six data points and four degrees of freedom). This value is probably affected by the fact that we are assuming constant initial data, while the energy slightly changes between simulations. Let us emphasize that we could not extract a meaningful value for the $\theta^{\rm fit}_{\chi_-^2}$ coefficient, consistently with our finding that these effects are subdominant (even for higher spin values).

TABLE VI. Small-spin dependence of the scattering angle for $\hat{E}_{\rm in} \simeq 1.02264$ and $\hat{L}_{\rm in} \simeq 1.1456$. PM predictions for the different spin-orders (if available) together with values extracted by fitting NR data [Eq. (C2)].

	3PM	4PM	$w^{\rm eob}_{\rm 3PM}$	$w^{\rm eob}_{\rm 4PM}$	NR
θ_0	2.255	2.519	3.543	3.920	3.872 ± 0.048
θ_{χ_+}	−0.433	−0.621	−2.895	−4.221	-4.211 ± 0.031
$\theta_{\chi_+^2}$	0.085	⋯	3.898	7.904	8.75 ± 0.60
$\theta_{\chi_-^2}$	−0.001	⋯	0.034	0.198	0.6 ± 3.1

In Table VI we compare these NR-fitting coefficients to their (PM-expanded and $w^{\rm eob}$-resummed) analytical analogs. In order to extract $w^{\rm eob}_{\rm 3PM}$ and $w^{\rm eob}_{\rm 4PM}$ (not including 4PM spin-orbit terms), we repeat the same fitting procedure employed for the NR angles (but setting the initial energy to the constant, average, value). For the considered initial data, $(\hat{E}_{\rm in}, \hat{L}_{\rm in}) \simeq (1.02264, 1.1456)$, the PM-expanded predictions are not satisfactory, as could be deduced from Fig. 6. The successive PM orders show a slow convergence towards the numerical results. The EOB-resummed equivalents, instead, are in good agreement with the numerical estimates, with the $w^{\rm eob}_{\rm 4PM}$ values mostly agreeing within one standard deviation with the NR ones.

[1] B. P. Abbott *et al.* (LIGO Scientific and Virgo Collaborations), GWTC-1: A gravitational-wave transient catalog of compact binary mergers observed by LIGO and Virgo during the first and second observing runs, Phys. Rev. X **9**, 031040 (2019).

[2] R. Abbott *et al.* (LIGO Scientific and Virgo Collaborations), GWTC-2: Compact binary coalescences observed by LIGO and Virgo during the first half of the third observing run, Phys. Rev. X **11**, 021053 (2021).

[3] R. Abbott *et al.* (LIGO Scientific, VIRGO, and KAGRA Collaborations), Tests of general relativity with GWTC-3, arXiv:2111.03606 [Phys. Rev. D (to be published)].

[4] Alexander H. Nitz, Sumit Kumar, Yi-Fan Wang, Shilpa Kastha, Shichao Wu, Marlin Schäfer, Rahul Dhurkunde, and Collin D. Capano, 4-OGC: Catalog of gravitational waves from compact binary mergers, Astrophys. J. **946**, 59 (2023).

[5] Seth Olsen, Tejaswi Venumadhav, Jonathan Mushkin, Javier Roulet, Barak Zackay, and Matias Zaldarriaga, New binary black hole mergers in the LIGO-Virgo O3a data, Phys. Rev. D **106**, 043009 (2022).

[6] Frans Pretorius, Evolution of binary black hole spacetimes, Phys. Rev. Lett. **95**, 121101 (2005).

[7] Manuela Campanelli, C. O. Lousto, P. Marronetti, and Y. Zlochower, Accurate evolutions of orbiting black-hole binaries without excision, Phys. Rev. Lett. **96**, 111101 (2006).

[8] Abdul H. Mroue, Mark A. Scheel, Bela Szilagyi, Harald P. Pfeiffer, Michael Boyle *et al.*, A catalog of 174 binary black-hole simulations for gravitational-wave astronomy, Phys. Rev. Lett. **111**, 241104 (2013).

[9] Sascha Husa, Sebastian Khan, Mark Hannam, Michael Pürrer, Frank Ohme, Xisco Jiménez Forteza, and Alejandro Bohé, Frequency-domain gravitational waves from nonprecessing black-hole binaries. I. New numerical waveforms and anatomy of the signal, Phys. Rev. D **93**, 044006 (2016).

[10] Karan Jani, James Healy, James A. Clark, Lionel London, Pablo Laguna, and Deirdre Shoemaker, Georgia tech

catalog of gravitational waveforms, Classical Quantum Gravity **33**, 204001 (2016).
[11] Michael Boyle *et al.*, The SXS Collaboration catalog of binary black hole simulations, Classical Quantum Gravity **36**, 195006 (2019).
[12] James Healy, Carlos O. Lousto, Jacob Lange, Richard O'Shaughnessy, Yosef Zlochower, and Manuela Campanelli, Second RIT binary black hole simulations catalog and its application to gravitational waves parameter estimation, Phys. Rev. D **100**, 024021 (2019).
[13] Eleanor Hamilton *et al.*, A catalogue of precessing black-hole-binary numerical-relativity simulations, arXiv:2303.05419.
[14] Scott E. Field, Chad R. Galley, Jan S. Hesthaven, Jason Kaye, and Manuel Tiglio, Fast prediction and evaluation of gravitational waveforms using surrogate models, Phys. Rev. X **4**, 031006 (2014).
[15] Jonathan Blackman, Scott E. Field, Mark A. Scheel, Chad R. Galley, Daniel A. Hemberger, Patricia Schmidt, and Rory Smith, A surrogate model of gravitational waveforms from numerical relativity simulations of precessing binary black hole mergers, Phys. Rev. D **95**, 104023 (2017).
[16] Vijay Varma, Scott E. Field, Mark A. Scheel, Jonathan Blackman, Davide Gerosa, Leo C. Stein, Lawrence E. Kidder, and Harald P. Pfeiffer, Surrogate models for precessing binary black hole simulations with unequal masses, Phys. Rev. Res. **1**, 033015 (2019).
[17] A. Buonanno and T. Damour, Effective one-body approach to general relativistic two-body dynamics, Phys. Rev. D **59**, 084006 (1999).
[18] Alessandra Buonanno and Thibault Damour, Transition from inspiral to plunge in binary black hole coalescences, Phys. Rev. D **62**, 064015 (2000).
[19] Rossella Gamba, Sarp Akçay, Sebastiano Bernuzzi, and Jake Williams, Effective-one-body waveforms for precessing coalescing compact binaries with post-Newtonian twist, Phys. Rev. D **106**, 024020 (2022).
[20] Serguei Ossokine *et al.*, Multipolar effective-one-body waveforms for precessing binary black holes: Construction and validation, Phys. Rev. D **102**, 044055 (2020).
[21] Antoni Ramos-Buades, Alessandra Buonanno, Héctor Estellés, Mohammed Khalil, Deyan P. Mihaylov, Serguei Ossokine, Lorenzo Pompili, and Mahlet Shiferaw, Next generation of accurate and efficient multipolar precessing-spin effective-one-body waveforms for binary black holes, arXiv:2303.18046 [Phys. Rev. D (to be published)].
[22] Mark Hannam, Patricia Schmidt, Alejandro Bohé, Leila Haegel, Sascha Husa, Frank Ohme, Geraint Pratten, and Michael Pürrer, Simple model of complete precessing black-hole-binary gravitational waveforms, Phys. Rev. Lett. **113**, 151101 (2014).
[23] Geraint Pratten, Sascha Husa, Cecilio Garcia-Quiros, Marta Colleoni, Antoni Ramos-Buades, Hector Estelles, and Rafel Jaume, Setting the cornerstone for a family of models for gravitational waves from compact binaries: The dominant harmonic for nonprecessing quasicircular black holes, Phys. Rev. D **102**, 064001 (2020).
[24] Cecilio García-Quirós, Marta Colleoni, Sascha Husa, Héctor Estellés, Geraint Pratten, Antoni Ramos-Buades, Maite Mateu-Lucena, and Rafel Jaume, Multimode frequency-domain model for the gravitational wave signal from nonprecessing black-hole binaries, Phys. Rev. D **102**, 064002 (2020).
[25] Geraint Pratten *et al.*, Computationally efficient models for the dominant and subdominant harmonic modes of precessing binary black holes, Phys. Rev. D **103**, 104056 (2021).
[26] Eleanor Hamilton, Lionel London, Jonathan E. Thompson, Edward Fauchon-Jones, Mark Hannam, Chinmay Kalaghatgi, Sebastian Khan, Francesco Pannarale, and Alex Vano-Vinuales, Model of gravitational waves from precessing black-hole binaries through merger and ringdown, Phys. Rev. D **104**, 124027 (2021).
[27] L. Blanchet and T. Damour, Postnewtonian generation of gravitational waves, Ann. Inst. Henri Poincaré Phys. Theor. **50**, 377 (1989), https://inspirehep.net/literature/287863.
[28] Luc Blanchet, Gravitational radiation from post-Newtonian sources and inspiralling compact binaries, Living Rev. Relativity **17**, 2 (2014).
[29] Thibault Damour, Piotr Jaranowski, and Gerhard Schäfer, Nonlocal-in-time action for the fourth post-Newtonian conservative dynamics of two-body systems, Phys. Rev. D **89**, 064058 (2014).
[30] Michele Levi and Jan Steinhoff, Next-to-next-to-leading order gravitational spin-orbit coupling via the effective field theory for spinning objects in the post-Newtonian scheme, J. Cosmol. Astropart. Phys. 01 (2016) 011.
[31] Donato Bini and Thibault Damour, Gravitational scattering of two black holes at the fourth post-Newtonian approximation, Phys. Rev. D **96**, 064021 (2017).
[32] Gerhard Schaefer and Piotr Jaranowski, Hamiltonian formulation of general relativity and post-Newtonian dynamics of compact binaries, Living Rev. Relativity **21**, 7 (2018).
[33] Donato Bini, Thibault Damour, and Andrea Geralico, Novel approach to binary dynamics: Application to the fifth post-Newtonian level, Phys. Rev. Lett. **123**, 231104 (2019).
[34] Donato Bini, Thibault Damour, and Andrea Geralico, Binary dynamics at the fifth and fifth-and-a-half post-Newtonian orders, Phys. Rev. D **102**, 024062 (2020).
[35] Donato Bini, Thibault Damour, and Andrea Geralico, Sixth post-Newtonian local-in-time dynamics of binary systems, Phys. Rev. D **102**, 024061 (2020).
[36] Donato Bini, Thibault Damour, and Andrea Geralico, Sixth post-Newtonian nonlocal-in-time dynamics of binary systems, Phys. Rev. D **102**, 084047 (2020).
[37] Andrea Antonelli, Chris Kavanagh, Mohammed Khalil, Jan Steinhoff, and Justin Vines, Gravitational spin-orbit and aligned $\mathrm{spin}_1 - \mathrm{spin}_2$ couplings through third-subleading post-Newtonian orders, Phys. Rev. D **102**, 124024 (2020).
[38] J. Blümlein, A. Maier, P. Marquard, and G. Schäfer, The fifth-order post-Newtonian Hamiltonian dynamics of two-body systems from an effective field theory approach: Potential contributions, Nucl. Phys. **B965**, 115352 (2021).
[39] J. Blümlein, A. Maier, P. Marquard, and G. Schäfer, The fifth-order post-Newtonian Hamiltonian dynamics of two-body systems from an effective field theory approach, Nucl. Phys. **B983**, 115900 (2022).

[40] Manoj K. Mandal, Pierpaolo Mastrolia, Raj Patil, and Jan Steinhoff, Gravitational spin-orbit Hamiltonian at NNNLO in the post-Newtonian framework, J. High Energy Phys. 03 (2023) 130.
[41] Manoj K. Mandal, Pierpaolo Mastrolia, Raj Patil, and Jan Steinhoff, Gravitational quadratic-in-spin Hamiltonian at NNNLO in the post-Newtonian framework, J. High Energy Phys. 07 (2023) 128.
[42] David Reitze *et al.*, Cosmic explorer: The U.S. contribution to gravitational-wave astronomy beyond LIGO, Bull. Am. Astron. Soc. **51**, 035 (2019), https://inspirehep.net/literature/1743201.
[43] M. Punturo, M. Abernathy, F. Acernese, B. Allen, N. Andersson *et al.*, The Einstein telescope: A third-generation gravitational wave observatory, Classical Quantum Gravity **27**, 194002 (2010).
[44] Pau Amaro-Seoane *et al.* (LISA Collaboration), Laser interferometer space antenna, arXiv:1702.00786.
[45] Isobel M. Romero-Shaw, Paul D. Lasky, Eric Thrane, and Juan Calderon Bustillo, GW190521: orbital eccentricity and signatures of dynamical formation in a binary black hole merger signal, Astrophys. J. Lett. **903**, L5 (2020).
[46] Juan Calderón Bustillo, Nicolas Sanchis-Gual, Alejandro Torres-Forné, and José A. Font, Confusing head-on collisions with precessing intermediate-mass binary black hole mergers, Phys. Rev. Lett. **126**, 201101 (2021).
[47] V. Gayathri, J. Healy, J. Lange, B. O'Brien, M. Szczepanczyk, Imre Bartos, M. Campanelli, S. Klimenko, C. O. Lousto, and R. O'Shaughnessy, Eccentricity estimate for black hole mergers with numerical relativity simulations, Nat. Astron. **6**, 344 (2022).
[48] Rossella Gamba, Matteo Breschi, Gregorio Carullo, Piero Rettegno, Simone Albanesi, Sebastiano Bernuzzi, and Alessandro Nagar, GW190521 as a dynamical capture of two nonspinning black holes, Nat. Astron. **7**, 11 (2023).
[49] Ryan M. O'Leary, Frederic A. Rasio, John M. Fregeau, Natalia Ivanova, and Richard W. O'Shaughnessy, Binary mergers and growth of black holes in dense star clusters, Astrophys. J. **637**, 937 (2006).
[50] Ryan M. O'Leary, Bence Kocsis, and Abraham Loeb, Gravitational waves from scattering of stellar-mass black holes in galactic nuclei, Mon. Not. R. Astron. Soc. **395**, 2127 (2009).
[51] Johan Samsing, Morgan MacLeod, and Enrico Ramirez-Ruiz, The formation of eccentric compact binary inspirals and the role of gravitational wave emission in binary-single stellar encounters, Astrophys. J. **784**, 71 (2014).
[52] Carl L. Rodriguez, Sourav Chatterjee, and Frederic A. Rasio, Binary black hole mergers from globular clusters: Masses, merger rates, and the impact of stellar evolution, Phys. Rev. D **93**, 084029 (2016).
[53] Krzysztof Belczynski, Daniel E. Holz, Tomasz Bulik, and Richard O'Shaughnessy, The first gravitational-wave source from the isolated evolution of two 40-100 Msun stars, Nature (London) **534**, 512 (2016).
[54] Johan Samsing, Eccentric black hole mergers forming in globular clusters, Phys. Rev. D **97**, 103014 (2018).
[55] Isobel M. Romero-Shaw, Paul D. Lasky, and Eric Thrane, Searching for eccentricity: Signatures of dynamical formation in the first gravitational-wave transient catalogue of LIGO and Virgo, Mon. Not. R. Astron. Soc. **490**, 5210 (2019).
[56] Michael Zevin, Isobel M. Romero-Shaw, Kyle Kremer, Eric Thrane, and Paul D. Lasky, Implications of eccentric observations on binary black hole formation channels, Astrophys. J. Lett. **921**, L43 (2021).
[57] Thibault Damour, Gravitational scattering, post-Minkowskian approximation and effective one-body theory, Phys. Rev. D **94**, 104015 (2016).
[58] Thibault Damour, High-energy gravitational scattering and the general relativistic two-body problem, Phys. Rev. D **97**, 044038 (2018).
[59] Clifford Cheung, Ira Z. Rothstein, and Mikhail P. Solon, From scattering amplitudes to classical potentials in the post-Minkowskian expansion, Phys. Rev. Lett. **121**, 251101 (2018).
[60] Alfredo Guevara, Alexander Ochirov, and Justin Vines, Scattering of spinning black holes from exponentiated soft factors, J. High Energy Phys. 09 (2019) 056.
[61] David A. Kosower, Ben Maybee, and Donal O'Connell, Amplitudes, observables, and classical scattering, J. High Energy Phys. 02 (2019) 137.
[62] Zvi Bern, Clifford Cheung, Radu Roiban, Chia-Hsien Shen, Mikhail P. Solon, and Mao Zeng, Scattering amplitudes and the conservative Hamiltonian for binary systems at third post-Minkowskian order, Phys. Rev. Lett. **122**, 201603 (2019).
[63] Zvi Bern, Clifford Cheung, Radu Roiban, Chia-Hsien Shen, Mikhail P. Solon, and Mao Zeng, Black hole binary dynamics from the double copy and effective theory, J. High Energy Phys. 10 (2019) 206.
[64] N. E. J. Bjerrum-Bohr, Andrea Cristofoli, and Poul H. Damgaard, Post-Minkowskian scattering angle in Einstein gravity, J. High Energy Phys. 08 (2020) 038.
[65] Enrico Herrmann, Julio Parra-Martinez, Michael S. Ruf, and Mao Zeng, Radiative classical gravitational observables at $\mathcal{O}(\mathrm{G}^3)$ from scattering amplitudes, J. High Energy Phys. 10 (2021) 148.
[66] Zvi Bern, Julio Parra-Martinez, Radu Roiban, Michael S. Ruf, Chia-Hsien Shen, Mikhail P. Solon, and Mao Zeng, Scattering amplitudes and conservative binary dynamics at $\mathcal{O}(G^4)$, Phys. Rev. Lett. **126**, 171601 (2021).
[67] Zvi Bern, Julio Parra-Martinez, Radu Roiban, Michael S. Ruf, Chia-Hsien Shen, Mikhail P. Solon, and Mao Zeng, Scattering amplitudes, the tail effect, and conservative binary dynamics at O(G4), Phys. Rev. Lett. **128**, 161103 (2022).
[68] N. Emil J. Bjerrum-Bohr, Poul H. Damgaard, Ludovic Planté, and Pierre Vanhove, The amplitude for classical gravitational scattering at third post-Minkowskian order, J. High Energy Phys. 08 (2021) 172.
[69] Aneesh V. Manohar, Alexander K. Ridgway, and Chia-Hsien Shen, Radiated angular momentum and dissipative effects in classical scattering, Phys. Rev. Lett. **129**, 121601 (2022).
[70] M. V. S. Saketh, Justin Vines, Jan Steinhoff, and Alessandra Buonanno, Conservative and radiative dynamics in classical relativistic scattering and bound systems, Phys. Rev. Res. **4**, 013127 (2022).

[71] Arnau Koemans Collado, Paolo Di Vecchia, and Rodolfo Russo, Revisiting the second post-Minkowskian eikonal and the dynamics of binary black holes, Phys. Rev. D **100**, 066028 (2019).
[72] Paolo Di Vecchia, Stephen G. Naculich, Rodolfo Russo, Gabriele Veneziano, and Chris D. White, A tale of two exponentiations in $\mathcal{N} = 8$ supergravity at subleading level, J. High Energy Phys. 03 (2020) 173.
[73] Paolo Di Vecchia, Carlo Heissenberg, Rodolfo Russo, and Gabriele Veneziano, The eikonal approach to gravitational scattering and radiation at $\mathcal{O}(G^3)$, J. High Energy Phys. 07 (2021) 169.
[74] Paolo Di Vecchia, Carlo Heissenberg, Rodolfo Russo, and Gabriele Veneziano, The eikonal operator at arbitrary velocities I: The soft-radiation limit, J. High Energy Phys. 07 (2022) 039.
[75] Gregor Kälin and Rafael A. Porto, Post-Minkowskian effective field theory for conservative binary dynamics, J. High Energy Phys. 11 (2020) 106.
[76] Gregor Kälin, Zhengwen Liu, and Rafael A. Porto, Conservative dynamics of binary systems to third post-Minkowskian order from the effective field theory approach, Phys. Rev. Lett. **125**, 261103 (2020).
[77] Stavros Mougiakakos, Massimiliano Maria Riva, and Filippo Vernizzi, Gravitational Bremsstrahlung in the post-Minkowskian effective field theory, Phys. Rev. D **104**, 024041 (2021).
[78] Christoph Dlapa, Gregor Kälin, Zhengwen Liu, and Rafael A. Porto, Dynamics of binary systems to fourth Post-Minkowskian order from the effective field theory approach, Phys. Lett. B **831**, 137203 (2022).
[79] Christoph Dlapa, Gregor Kälin, Zhengwen Liu, and Rafael A. Porto, Conservative dynamics of binary systems at fourth post-Minkowskian order in the large-eccentricity expansion, Phys. Rev. Lett. **128**, 161104 (2022).
[80] Gregor Kälin, Jakob Neef, and Rafael A. Porto, Radiation-reaction in the effective field theory approach to post-Minkowskian dynamics, J. High Energy Phys. 01 (2023) 140.
[81] Christoph Dlapa, Gregor Kälin, Zhengwen Liu, Jakob Neef, and Rafael A. Porto, Radiation reaction and gravitational waves at fourth post-Minkowskian order, Phys. Rev. Lett. **130**, 101401 (2023).
[82] Gustav Mogull, Jan Plefka, and Jan Steinhoff, Classical black hole scattering from a worldline quantum field theory, J. High Energy Phys. 02 (2021) 048.
[83] Massimiliano Maria Riva and Filippo Vernizzi, Radiated momentum in the post-Minkowskian worldline approach via reverse unitarity, J. High Energy Phys. 11 (2021) 228.
[84] Gustav Uhre Jakobsen, Gustav Mogull, Jan Plefka, and Jan Steinhoff, Classical gravitational bremsstrahlung from a worldline quantum field theory, Phys. Rev. Lett. **126**, 201103 (2021).
[85] Gustav Uhre Jakobsen, Gustav Mogull, Jan Plefka, and Benjamin Sauer, All things retarded: Radiation-reaction in worldline quantum field theory, J. High Energy Phys. 10 (2022) 128.
[86] Donato Bini, Thibault Damour, and Andrea Geralico, Radiative contributions to gravitational scattering, Phys. Rev. D **104**, 084031 (2021).
[87] Donato Bini and Thibault Damour, Radiation-reaction and angular momentum loss at the second post-Minkowskian order, Phys. Rev. D **106**, 124049 (2022).
[88] Donato Bini, Thibault Damour, and Andrea Geralico, Radiated momentum and radiation reaction in gravitational two-body scattering including time-asymmetric effects, Phys. Rev. D **107**, 024012 (2023).
[89] Danilo Chiaramello and Alessandro Nagar, Faithful analytical effective-one-body waveform model for spin-aligned, moderately eccentric, coalescing black hole binaries, Phys. Rev. D **101**, 101501 (2020).
[90] Alessandro Nagar, Alice Bonino, and Piero Rettegno, Effective one-body multipolar waveform model for spin-aligned, quasicircular, eccentric, hyperbolic black hole binaries, Phys. Rev. D **103**, 104021 (2021).
[91] Andrea Placidi, Simone Albanesi, Alessandro Nagar, Marta Orselli, Sebastiano Bernuzzi, and Gianluca Grignani, Exploiting Newton-factorized, 2PN-accurate waveform multipoles in effective-one-body models for spin-aligned noncircularized binaries, Phys. Rev. D **105**, 104030 (2022).
[92] Mohammed Khalil, Alessandra Buonanno, Jan Steinhoff, and Justin Vines, Radiation-reaction force and multipolar waveforms for eccentric, spin-aligned binaries in the effective-one-body formalism, Phys. Rev. D **104**, 024046 (2021).
[93] Antoni Ramos-Buades, Alessandra Buonanno, Mohammed Khalil, and Serguei Ossokine, Effective-one-body multipolar waveforms for eccentric binary black holes with nonprecessing spins, Phys. Rev. D **105**, 044035 (2022).
[94] Alessandro Nagar and Piero Rettegno, Next generation: Impact of high-order analytical information on effective one body waveform models for noncircularized, spin-aligned black hole binaries, Phys. Rev. D **104**, 104004 (2021).
[95] Mohammed Khalil, Alessandra Buonanno, Jan Steinhoff, and Justin Vines, Energetics and scattering of gravitational two-body systems at fourth post-Minkowskian order, Phys. Rev. D **106**, 024042 (2022).
[96] Ian Hinder, Frank Herrmann, Pablo Laguna, and Deirdre Shoemaker, Comparisons of eccentric binary black hole simulations with post-Newtonian models, Phys. Rev. D **82**, 024033 (2010).
[97] Roman Gold, Sebastiano Bernuzzi, Marcus Thierfelder, Bernd Brügmann, and Frans Pretorius, Eccentric binary neutron star mergers, Phys. Rev. D **86**, 121501 (2012).
[98] Adam G. M. Lewis, Aaron Zimmerman, and Harald P. Pfeiffer, Fundamental frequencies and resonances from eccentric and precessing binary black hole inspirals, Classical Quantum Gravity **34**, 124001 (2017).
[99] Antoni Ramos-Buades, Sascha Husa, Geraint Pratten, Héctor Estellés, Cecilio García-Quirós, Maite Mateu-Lucena, Marta Colleoni, and Rafel Jaume, First survey of spinning eccentric black hole mergers: Numerical relativity simulations, hybrid waveforms, and parameter estimation, Phys. Rev. D **101**, 083015 (2020).
[100] E. A. Huerta *et al.*, Physics of eccentric binary black hole mergers: A numerical relativity perspective, Phys. Rev. D **100**, 064003 (2019).
[101] Sarah Habib and E. A. Huerta, Characterization of numerical relativity waveforms of eccentric binary black hole mergers, Phys. Rev. D **100**, 044016 (2019).

[102] Tousif Islam, Vijay Varma, Jackie Lodman, Scott E. Field, Gaurav Khanna, Mark A. Scheel, Harald P. Pfeiffer, Davide Gerosa, and Lawrence E. Kidder, Eccentric binary black hole surrogate models for the gravitational waveform and remnant properties: Comparable mass, nonspinning case, Phys. Rev. D **103**, 064022 (2021).

[103] Antoni Ramos-Buades, Maarten van de Meent, Harald P. Pfeiffer, Hannes R. Rüter, Mark A. Scheel, Michael Boyle, and Lawrence E. Kidder, Eccentric binary black holes: Comparing numerical relativity and small mass-ratio perturbation theory, Phys. Rev. D **106**, 124040 (2022).

[104] Masaru Shibata, Hirotada Okawa, and Tetsuro Yamamoto, High-velocity collision of two black holes, Phys. Rev. D **78**, 101501 (2008).

[105] Ulrich Sperhake, Vitor Cardoso, Frans Pretorius, Emanuele Berti, Tanja Hinderer, and Nicolas Yunes, Cross section, final spin and zoom-whirl behavior in high-energy black hole collisions, Phys. Rev. Lett. **103**, 131102 (2009).

[106] Thibault Damour, Federico Guercilena, Ian Hinder, Seth Hopper, Alessandro Nagar, and Luciano Rezzolla, Strong-field scattering of two black holes: Numerics versus analytics, Phys. Rev. D **89**, 081503 (2014).

[107] Seth Hopper, Alessandro Nagar, and Piero Rettegno, Strong-field scattering of two spinning black holes: Numerics versus analytics, Phys. Rev. D **107**, 124034 (2023).

[108] James Healy and Carlos O. Lousto, Ultimate black hole recoil: What is the maximum high-energy collision kick?, Phys. Rev. Lett. **131**, 071401 (2023).

[109] Roland Haas *et al.*, The EINSTEIN TOOLKIT (2022), to find out more, visit http://einsteintoolkit.org.

[110] Jeffrey M. Bowen and James W. York, Jr., Time asymmetric initial data for black holes and black hole collisions, Phys. Rev. D **21**, 2047 (1980).

[111] Steven Brandt and Bernd Brügmann, A simple construction of initial data for multiple black holes, Phys. Rev. Lett. **78**, 3606 (1997).

[112] Marcus Ansorg, Bernd Brügmann, and Wolfgang Tichy, A single-domain spectral method for black hole puncture data, Phys. Rev. D **70**, 064011 (2004).

[113] Miguel Alcubierre, Bernd Brügmann, Peter Diener, Michael Koppitz, Denis Pollney, Edward Seidel, and Ryoji Takahashi, Gauge conditions for long term numerical black hole evolutions without excision, Phys. Rev. D **67**, 084023 (2003).

[114] Pedro Marronetti, Wolfgang Tichy, Bernd Brügmann, Jose Gonzalez, and Ulrich Sperhake, High-spin binary black hole mergers, Phys. Rev. D **77**, 064010 (2008).

[115] M. Shibata and T. Nakamura, Evolution of three-dimensional gravitational waves: Harmonic slicing case, Phys. Rev. D **52**, 5428 (1995).

[116] Thomas W. Baumgarte and Stuart L. Shapiro, On the numerical integration of Einstein's field equations, Phys. Rev. D **59**, 024007 (1999).

[117] T. Nakamura, K. Oohara, and Y. Kojima, General relativistic collapse to black holes and gravitational waves from black holes, Prog. Theor. Phys. Suppl. **90**, 1 (1987).

[118] J. David Brown, Peter Diener, Olivier Sarbach, Erik Schnetter, and Manuel Tiglio, Turduckening black holes: An Analytical and computational study, Phys. Rev. D **79**, 044023 (2009).

[119] John G. Baker, Joan Centrella, Dae-Il Choi, Michael Koppitz, and James van Meter, Gravitational wave extraction from an inspiraling configuration of merging black holes, Phys. Rev. Lett. **96**, 111102 (2006).

[120] Carles Bona, Joan Masso, Edward Seidel, and Joan Stela, A new formalism for numerical relativity, Phys. Rev. Lett. **75**, 600 (1995).

[121] H. O. Kreiss and J. Oliger, *Methods for the Approximate Solution of Time Dependent Problems* (International Council of Scientific Unions, World Meteorological Organization, Geneva, 1973), https://library.wmo.int/records/item/29240-methods-for-the-approximate-solution-of-time-dependent-problems.

[122] Denis Pollney, Christian Reisswig, Erik Schnetter, Nils Dorband, and Peter Diener, High accuracy binary black hole simulations with an extended wave zone, Phys. Rev. D **83**, 044045 (2011).

[123] Jonathan Thornburg, A fast apparent horizon finder for three-dimensional Cartesian grids in numerical relativity, Classical Quantum Gravity **21**, 743 (2004).

[124] Olaf Dreyer, Badri Krishnan, Deirdre Shoemaker, and Erik Schnetter, Introduction to isolated horizons in numerical relativity, Phys. Rev. D **67**, 024018 (2003).

[125] Gabrielle Allen, Peter Diener, Erik Schnetter, Frank Loeffler, Michael Thomas, Steven R. Brandt, and Ian Hinder, Simulation factory, https://simfactory.org/, accessed: 2023-01-05.

[126] Ian Hinder and Barry Wardell, https://simulationtools.org/.

[127] Douglas M. Eardley and Steven B. Giddings, Classical black hole production in high-energy collisions, Phys. Rev. D **66**, 044011 (2002).

[128] Hirotaka Yoshino and Yasusada Nambu, Black hole formation in the grazing collision of high-energy particles, Phys. Rev. D **67**, 024009 (2003).

[129] Steven B. Giddings and Vyacheslav S. Rychkov, Black holes from colliding wavepackets, Phys. Rev. D **70**, 104026 (2004).

[130] D. Amati, M. Ciafaloni, and G. Veneziano, Towards an S-matrix description of gravitational collapse, J. High Energy Phys. 02 (2008) 049.

[131] Frans Pretorius and Deepak Khurana, Black hole mergers and unstable circular orbits, Classical Quantum Gravity **24**, S83 (2007).

[132] Ulrich Sperhake, Emanuele Berti, Vitor Cardoso, and Frans Pretorius, Universality, maximum radiation and absorption in high-energy collisions of black holes with spin, Phys. Rev. Lett. **111**, 041101 (2013).

[133] Thibault Damour and Piero Rettegno, Strong-field scattering of two black holes: Numerical relativity meets post-Minkowskian gravity, Phys. Rev. D **107**, 064051 (2023).

[134] Thibault Damour, Coalescence of two spinning black holes: An effective one- body approach, Phys. Rev. D **64**, 124013 (2001).

[135] Manuela Campanelli, C. O. Lousto, and Y. Zlochower, Spinning-black-hole binaries: The orbital hang up, Phys. Rev. D **74**, 041501 (2006).

[136] Donato Bini and Thibault Damour, Gravitational spin-orbit coupling in binary systems, post-Minkowskian approximation and effective one-body theory, Phys. Rev. D **96**, 104038 (2017).

[137] Donato Bini and Thibault Damour, Gravitational spin-orbit coupling in binary systems at the second post-Minkowskian approximation, Phys. Rev. D **98**, 044036 (2018).
[138] Justin Vines, Scattering of two spinning black holes in post-Minkowskian gravity, to all orders in spin, and effective-one-body mappings, Classical Quantum Gravity **35**, 084002 (2018).
[139] Justin Vines, Jan Steinhoff, and Alessandra Buonanno, Spinning-black-hole scattering and the test-black-hole limit at second post-Minkowskian order, Phys. Rev. D **99**, 064054 (2019).
[140] Alfredo Guevara, Alexander Ochirov, and Justin Vines, Black-hole scattering with general spin directions from minimal-coupling amplitudes, Phys. Rev. D **100**, 104024 (2019).
[141] Gregor Kälin and Rafael A. Porto, From boundary data to bound states. Part II. Scattering angle to dynamical invariants (with twist), J. High Energy Phys. 02 (2020) 120.
[142] Dimitrios Kosmopoulos and Andres Luna, Quadratic-in-spin Hamiltonian at $\mathcal{O}(G^2)$ from scattering amplitudes, J. High Energy Phys. 07 (2021) 037.
[143] Wei-Ming Chen, Ming-Zhi Chung, Yu-tin Huang, and Jung-Wook Kim, The 2PM Hamiltonian for binary Kerr to quartic in spin, J. High Energy Phys. 08 (2022) 148.
[144] Rafael Aoude, Kays Haddad, and Andreas Helset, Classical gravitational spinning-spinless scattering at $O(G2S\infty)$, Phys. Rev. Lett. **129**, 141102 (2022).
[145] Gustav Uhre Jakobsen and Gustav Mogull, Conservative and radiative dynamics of spinning bodies at third post-Minkowskian order using worldline quantum field theory, Phys. Rev. Lett. **128**, 141102 (2022).
[146] Zvi Bern, Andres Luna, Radu Roiban, Chia-Hsien Shen, and Mao Zeng, Spinning black hole binary dynamics, scattering amplitudes, and effective field theory, Phys. Rev. D **104**, 065014 (2021).
[147] Zvi Bern, Dimitrios Kosmopoulos, Andrés Luna, Radu Roiban, and Fei Teng, Binary dynamics through the fifth power of spin at O(G2), Phys. Rev. Lett. **130**, 201402 (2023).
[148] Fernando Febres Cordero, Manfred Kraus, Guanda Lin, Michael S. Ruf, and Mao Zeng, Conservative binary dynamics with a spinning black hole at O(G3) from scattering amplitudes, Phys. Rev. Lett. **130**, 021601 (2023).
[149] Francesco Alessio and Paolo Di Vecchia, Radiation reaction for spinning black-hole scattering, Phys. Lett. B **832**, 137258 (2022).
[150] Francesco Alessio, Kerr binary dynamics from minimal coupling and double copy, arXiv:2303.12784.
[151] Gustav Uhre Jakobsen, Gustav Mogull, Jan Plefka, Benjamin Sauer, and Yingxuan Xu, Conservative scattering of spinning black holes at fourth post-Minkowskian order, Phys. Rev. Lett. **131**, 151401 (2023).
[152] Gustav Uhre Jakobsen, Gustav Mogull, Jan Plefka, and Benjamin Sauer, Dissipative scattering of spinning black holes at fourth post-Minkowskian order, arXiv:2308.11514.
[153] Thibault Damour, Piotr Jaranowski, and Gerhard Schaefer, On the determination of the last stable orbit for circular general relativistic binaries at the third postNewtonian approximation, Phys. Rev. D **62**, 084011 (2000).
[154] Thibault Damour, Classical and quantum scattering in post-Minkowskian gravity, Phys. Rev. D **102**, 024060 (2020).
[155] See Supplemental Material athttp://link.aps.org/supplemental/10.1103/PhysRevD.108.124016 the expressions of the EOB-resummed potentials w^{eob}, see Eq. (4.14).
[156] L. D. Landau and E. M. Lifshitz, *Mechanics (Volume 1)*, Course of Theoretical Physics (Pergamon Press, New York, 1960), https://books.google.fr/books?id=e-xASAehg1sC.
[157] Gregor Kälin and Rafael A. Porto, From boundary data to bound states, J. High Energy Phys. 01 (2020) 072.
[158] Andreas Brandhuber, Graham R. Brown, Gang Chen, Stefano De Angelis, Joshua Gowdy, and Gabriele Travaglini, One-loop gravitational bremsstrahlung and waveforms from a heavy-mass effective field theory, J. High Energy Phys. 06 (2023) 048.
[159] Aidan Herderschee, Radu Roiban, and Fei Teng, The sub-leading scattering waveform from amplitudes, J. High Energy Phys. 06 (2023) 004.
[160] Alessandro Georgoudis, Carlo Heissenberg, and Ingrid Vazquez-Holm, Inelastic exponentiation and classical gravitational scattering at one loop, J. High Energy Phys. 06 (2023) 126.
[161] Wolfgang Tichy, Bernd Bruegmann, and Pablo Laguna, Gauge conditions for binary black hole puncture data based on an approximate helical Killing vector, Phys. Rev. D **68**, 064008 (2003).